The influence of vegetation drought stress on formaldehyde and ozone distributions over a central European city

Heidelinde Trimmel [a,g,*], Paul Hamer [d], Monika Mayer [a], Stefan F. Schreier [a], Philipp Weihs [a], Josef Eitzinger [a], Hans Sandén [b], Anne Charlott Fitzky [b], Andreas Richter [c], Jean-Christophe Calvet [e], Bertrand Bonan [e], Catherine Meurey [e], Islen Vallejo [d], Sabine Eckhardt [d], Gabriela Sousa Santos [d], Safae Oumami [e], Joaquim Arteta [e], Virginie Marécal [e], Leonor Tarrasón [d], Thomas Karl [f], Harald E. Rieder [a]

[a] University of Natural Resources and Life Sciences, Vienna, Department of Water, Atmosphere and Environment, Institute of Meteorology and Climatology, Gregor-Mendel-Straße 33, 1180, Vienna, Austria
[b] University of Natural Resources and Life Sciences Vienna, Department of Forest and Soil Sciences, Institute of Forest Ecology, Peter-Jordan-Straße 82, 1190, Vienna, Austria
[c] Institute of Environmental Physics, University of Bremen, Germany
[d] NILU – Norwegian Institute for Air Research, INBY, PO Box 100, NO-2027, Kjeller, Norway
[e] Centre National de Recherches Météorologiques, Université de Toulouse, Météo-France, CNRS, Toulouse, France
[f] University of Innsbruck, Department of Atmospheric and Cryospheric Sciences, Innsbruck, Austria
[g] International Institute for Applied Systems Analysis (IIASA), Schloßplatz 1, 2361, Laxenburg, Austria

HIGHLIGHTS

- Spring-time precipitation deficit can reduce urban formaldehyde and ozone levels.
- Local drought may coincide with urban ozone increases due to advected isoprene.
- Emissions from adjacent forested areas are important for urban ozone formation.

ARTICLE INFO

ABSTRACT

To estimate the effect of vegetation stress and changes in biogenic volatile organic compound (BVOC) emissions on urban ozone (O_3) levels we perform a systematic, observation-based analysis of the relationship between formaldehyde (HCHO) mixing ratios, meteorological parameters, measurement-based drought indicators and O_3 over the central European city of Vienna, Austria. In addition, numerical models SURface EXternalisée (SURFEX), Model of Emissions of Gases and Aerosols from Nature (MEGAN) Vers.2.1 and 3 and MOdèle de Chimie A Grande Echelle (MOCAGE) are combined to estimate the soil moisture, the spatial distribution and drought response of isoprene emissions, and the resulting distribution of HCHO in the atmosphere. To analyse the effect of drought during spring and summer we contrast observations during dry and reference years. Our results show that the observed HCHO can be explained using the simulated isoprene emissions as well as observed and simulated vegetation drought responses. HCHO mixing ratios differ strongly between dry and reference seasons. Spring-time precipitation deficits facilitate reduced HCHO mixing ratios due to delayed and weakened plant growth. In consequence also O_3 burdens are lowered due to reduced BVOC precursor emissions. These reductions occur despite radiation levels being higher than during the reference year, illustrating the strong potential of spring-time BVOC emissions to modulate urban O_3 burdens. Conversely, during summer elevated O_3 levels occur during local drought conditions. These are driven by advected isoprene originating from nearby forest areas, which are not affected by drought. Our results regarding elevated summer-time O_3 burdens under vegetation heat and drought stress are in good agreement with previous work.

1. Introduction

Ground-level ozone (O_3) poses a serious threat to health for humans and vegetation (Cho et al., 2011; Emberson et al., 2007). Further, O_3 is an important short-lived greenhouse gas in the troposphere (IPCC, 2021; Checa-Garcia et al., 2018). O_3 is photochemically produced from precursor substances, most importantly nitrogen oxides (NO_x) and volatile organic compounds (VOCs) (Calfapietra et al., 2013). Production rates and peak O_3 levels depend on precursor levels, solar radiation, the O_3-deposition sink, and air temperatures. High O_3 levels are favoured by stable meteorological conditions caused by anticyclonic conditions, heat waves, and droughts (Lin et al., 2020). Land-atmosphere interactions such as soil moisture forcing can intensify and prolong weather extremes (Jia et al., 2019; Teng et al., 2019) and the role this plays in intensifying photochemical O_3 pollution is still not fully clear. In this study, we seek to address this question via a case study of summer and spring heat-waves and droughts in the region around Vienna, Austria.

Key O_3 precursor emissions of NO_x, non-methane volatile organic compounds (NMVOC) and methane (CH_4) have been reduced in the European Environmental Agency member countries and the UK (EEA-33) by 45%, 41% and 29%, respectively, between 2000 and 2018 (European Environment Agency, 2020). Despite these reductions, the exposure to elevated O_3 levels in urban environments remains substantial across Europe (Lin et al., 2020), and also in Austria (Mayer et al., 2022).

In addition to O_3 precursors emitted through anthropogenic activities, biogenic volatile organic compounds (BVOCs) are also extremely important O_3 precursors. BVOCs are mainly emitted by trees to communicate, as a response to biotic and abiotic stresses, and as a by-product during growth and senescence (Fares et al., 2010). The amount and composition of emitted BVOCs changes from species to species and depends on stresses, age, and location (Fitzky et al., 2023; van Meeningen et al., 2016). The emission of BVOCs, in particular isoprene and terpenes, represents an important source of precursors for formaldehyde (HCHO).

BVOC emissions depend on leaf area, photosynthetic active radiation (Bonn et al., 2019), and air temperature. In general, BVOC plant emissions increase when air temperatures rise (Bauwens et al., 2018; Fitzky et al., 2023; Ferracci et al., 2020). Due to the link between air temperature and isoprene emissions, climate change is expected to impact on future BVOC emissions. For example, Peñuelas and Staudt (2010) expect an increase of over 60% in isoprenoids for a rise in global air temperature of about 3 °C due to direct effects on the BVOCs producing metabolic pathways and indirect effects as prolonged growth season.

The role played by air temperature in controlling BVOC emissions also points to the potential for heat waves to lead to increases in BVOC emissions. However, prolonged elevated temperatures during a heat wave can lead to heat stress, which initially causes an increase in BVOC emissions but after a prolonged period leads to a reduction in emissions (Niinemets, 2010). Indeed, Kleist et al. (2012) document an irreversible decrease of monoterpenes, sesquiterpenes and phenolic biogenic volatile organic compounds independent of tree species caused by prolonged thermal stress. Heat stress likely leads to reductions in BVOC emissions through the mechanisms of reduced photosynthesis, increased photo-oxidative stress, and decreased growth rate of leaves until the point that leaves are shed.

Droughts can also strongly affect BVOC emissions. While BVOC emissions generally decrease during drought stress (Niinemets, 2010), uncertainties remain in current models concerning the precise response of BVOC emissions to drought (Seco et al., 2015), especially in the context of global warming (Peñuelas and Staudt, 2010). The effect of soil water availability on isoprene is strongly related to the biological growth type curve, but the sum of monoterpenes shows a hydraulic conductivity pattern which is controlled by the plant's stomata opening. For example, sesquiterpene emissions tend to increase until the wilting point is reached, which is the condition under which soil water is no longer available to the plant (Bonn et al., 2019). In another example, Zheng et al. (2017) found in flux tower measurements a 54% reduction in isoprene emissions during an anomalously dry July in Missouri, USA.

Extreme heat events and droughts can often occur concurrently, which means that the temperature effects of a heat wave often combine with those of drought effects. During such combined heat and drought events, BVOC emissions first increase (temperature-related) and once species-dependent thresholds are passed emissions drop significantly due to drought stress and their chemical composition changes (Bonn et al., 2019; Peron et al., 2021).

In addition to generally applicable drought and extreme heat effects, certain tree species can have species-specific responses that merit further mention due to their prevalence in the Vienna region. Species react differently to heat and drought stresses and some cool their leaves by increased stomatal conductance (Teskey et al., 2015) leading to species-dependent thresholds for emitting behaviour. Fitzky et al. (2023) found for laboratory drought conditions a general decrease in BVOC emissions for *Quercus robur* (except isoprene), *Fagus sylvatica*, *Carpinus betulus* and *Betula pendula* mainly caused by a drop in the oxygenated VOC (OVOC) methanol and hexenyl acetate emissions and less from other emitted compounds. Conversely, for the methanol emitting *Betula pendula* Fitzky et al. (2023) observed an increase in maximum assimilation during drought conditions. For isohydric *B. pendula*, which is known for fast drought response, the decrease in methanol was 54% under drought stress. Only the emissions of isoprene and monoterpene which are synthetized in the non-mevalonate metabolic pathway (MEP) are decoupled from photosynthesis and tended to increase using stored carbon (Fitzky et al., 2023). If the leaves are exposed to additional O_3 stress, isoprene emissions decrease for *Quercus robur* - which is the main emitter of BVOCs - under laboratory conditions, while monoterpene and sesquiterpene emissions increase during ongoing drought (Peron et al., 2021).

Commonly, ecotype specific standard emission potentials are defined and compiled based on ecotype level flux and species level lab measurements. These are used offline or coupled within atmospheric models in the Model of Emissions of Gases and Aerosols from Nature (MEGAN) (Guenther et al., 2012; Karl et al., 2009; Oderbolz et al., 2013; Scholz, 2019; Simpson et al., 1999). For Austria, the annual total biogenic VOC emissions contained in different vegetation inventories range between 8 and 16 Gg yr^{-1} isoprene, 32–91 Gg yr^{-1} monoterpenes, 3–4 Gg yr^{-1} sesquiterpene and 82–104 Gg yr^{-1} oxygenated volatile organic compounds (OVOC) (Oderbolz et al., 2013). These four compounds alone sum up to approximately 215 Gg yr^{-1}. Here alpine regions are included as well. We now compare the reported inventories of anthropogenic NMVOCs to the reported BVOC emissions in order to provide context for the relative contribution of both sources to VOC emissions in Austria. The anthropogenic NMVOC emissions reported for Austria (not including fuel export) on the other hand were only half of that (108 Gg yr^{-1}) in 2019 (Environment Agency Austria, 2021). While the anthropogenic emissions occur throughout the year, 30–40% of the annual biogenic emissions take place in July and 25–30% in June and August (Curci et al., 2010), which further reduces the anthropogenic share of the total emissions in the summer months. BVOC emissions are therefore dominant during the summer months dominant (~5 times greater than anthropogenic emissions) compared to the anthropogenic emissions within Austria. Apart from this VOCs from traffic, which is the main VOC pollutant source in the urban area are very low after the introduction of strong regulations compared to agricultural emissions. Potential anthropogenic sources close to Vienna are concentrated to the southwest. This aspect is further discussed in section 3.3.

HCHO can be used as a proxy for BVOC levels if direct measurements of the BVOCs themselves are unavailable. Globally, the main secondary source of HCHO, which is a short-lived high-yield oxidation product, is isoprene which forms a substantial portion (63–65% in temperate forests Guenther et al., 2012) of the emitted BVOCs. For this reason, HCHO has been widely used as a proxy for isoprene emissions mainly monitored

from space (Bauwens et al., 2016; Marais et al., 2014; Millet et al., 2008; Vigouroux et al., 2020), but also by using ground-based remote sensing with the long path (LP) and multi-axis (MAX) differential optical absorption spectroscopy (DOAS) techniques (MacDonald et al., 2012). Primary sources of HCHO itself are estimated to be minor in urban areas with a around 5% contribution (De Smedt et al., 2010; Fu et al., 2007; Palmer et al., 2003; Parrish et al., 2012; Schreier et al., 2020).

Apart from BVOC emissions contributing to O_3 production, O_3 deposition on vegetation areas can reduce atmospheric O_3 concentrations. Particularly within the NO_x limited urban O_3 regime, levels of O_3 deposition may differ significantly. Vegetation mainly takes up O_3 directly via their stomata or over their cuticula and stems. Further, there is ground uptake, whereas snow and wet surfaces limit O_3 deposition. While for dry leaves cuticular uptake is lower than for wet leaves, dry soil can take up more O_3 than wet soil (Clifton et al., 2020). Water-stressed plants have a reduced stomatal O_3 deposition, as their stomata close, which can reinforce high O_3 episodes (Lin et al., 2020). Demetillo et al. (2019) found in an observational analysis for the severe California drought 2011–2015 a 50% reduction of isoprene emissions, resulting in a 20% reduction in O_3 production. This reduction was offset by a reduced O_3 uptake by plants, which lead overall only to a 6% reduction in O_3 levels.

About 48% of Austria's area and 41% of the federal state surrounding Austria is covered with forests. Crowther et al. (2015) estimated an average tree density of about 367.22 trees/ha for Austria. Austria's capital Vienna, is surrounded by forests predominantly composed of tree species which are known as BVOCs emitters (Table S1). Vast forest areas are located in the mountainous regions west of Vienna (the so-called "Wienerwald") as well as Southeast of Vienna (the floodplain forests of Lobau). The surrounding forest districts (Bundesforschungszentrum für Wald, 2021; Karl et al., 2009) have a substantial share of the isoprene emitters such as *Quercus robur*, *Robinia pseudoacacia* and *Populus* sp. as well as the light and temperature-dependent monoterpene emitter *Fagus sylvatica* (Table S1).

For the City of Vienna, a detailed tree cadaster exists documenting the location, species, and specifics of trees located in public areas. For the urban, non-forested area of Vienna (339.972 km^2) 191 767 trees are registered in streets and parks according to Baumkataster Wien (City of Vienna, 2021), which yields a minimum density of 5.6 trees/ha, as trees on private property are not accounted for. The most abundant isoprene emitters, with over 1000 individuals and emission potentials of 12–70 µg gdw^{-1} h^{-1} are *Populus* sp., *Platanus x acerifolia*, *Robinia pseudoacacia*, *Koelreuteria paniculata* and *Quercus* sp. (Table S2: City of Vienna, 2021; Karl et al., 2009; Baghi et al., 2012; Nowak et al., 2002; Scholz, 2019). Monoterpene is mainly emitted by the over 16 000 *Aesculus sp.* and *Fagus sylvatica* trees (Table S2).

Comparing the amount of total BVOC emissions between *Quercus robur*, *Betula pendula* and *Fagus sylvatica/Carpinus betulus* gives the factors 100%, 0.06% and 0.02% respectively (Fitzky et al., 2023). While *Quercus robur* mainly emits isoprene (2-methyl-1,3-butadiene, C_5H_8; 97%), which is the dominant BVOC globally, *Fagus sylvatica* emits monoterpenes ($C_{10}H_{16}$; 80%) and *Betula pendula* and *Carpinus betulus* mainly emit the oxygenated BVOC methanol (CH_3OH; 72 and 60% respectively).

This study seeks to investigate the influence of BVOC emissions from trees on the surface ozone and HCHO burdens in the Vienna region. Specifically, we aim to answer the following research questions: (1) Are HCHO mixing ratios over Vienna during the growing season affected by changing emissions of BVOCs resulting of vegetation metabolism and photosynthetic activity? (2) Do heat and drought conditions affect HCHO mixing ratios over Vienna by changing emissions of BVOCs? (3) Are O_3 concentrations affected by heat and drought-stressed vegetation in Vienna?

2. Data and methods

To answer the questions detailed above, this study utilizes data from chemical trace gas measurements (HCHO mixing ratios, O_3 concentrations), meteorological measurements (air temperature, global radiation, wind speed, planetary boundary layer height) as well as ground based and satellite derived vegetation and drought indices. In addition, three types of numerical models are combined to estimate the soil moisture, the spatial distribution and drought response of isoprene emissions, and the resulting distribution of HCHO in the atmosphere.

2.1. Study area

The focus of research is the City of Vienna, with a population of about 2 million, and the surrounding areas that contribute to the emission of BVOCs and formation O_3 and HCHO. Apart from urban trees within the city area, Vienna is situated adjacent to different forest areas (Wienerwald to the west, Nationalpark Donauauen to the southeast), but also more distant forest areas (Fig. 1) may serve as potential BVOC sources to the city. The location of forest areas also including urban parks, and anthropogenic VOC sources are marked in Fig. 1.

Lifetimes of the emitted BVOCs (isoprene, monoterpenes, sesquiterpenes – half to 3 h) and HCHO (5 h, Arlander et al. (1995)) are sufficiently long with respect to typical transport times from forests to the city. Given the mean wind speed of 3.6 m/s in this area and not considering the less abundant sesquiterpenes (SQT) and oxygenated VOCs (OVOC) this amounts to a rough footprint area between 70 and 100 km influencing the HCHO concentrations measured in Vienna.

Vienna is characterized by a warm humid continental climate (Dfb according to the Köppen-Geiger classification) with warm summers and cold winters. The main wind directions (northwest and southeast) are similar for all the Viennese synoptic stations of the Austrian weather service (ZAMG) including stations in the rural east (Groβenzersdorf), the low-density urban area close to forested hills north of the city (Wien Hohe Warte) and city centre (Wien Innere Stadt). The soils within the footprint area are mainly loamy and characterized as dry to very dry (see Supplemental Figs. S1 and S2).

2.2. Meteorological and ozone data sets

We use a variety of meteorological covariates along with O_3 observations in this study (see Table 1). Air temperature (AT), sum of long wave and short wave downwelling ("global") radiation (GR), precipitation (PR), relative humidity (RH) and wind direction (WD) were obtained as 10-min data from the measurement station at the University of Natural Resources and Life Sciences, Vienna (BOKU; 48° 14′ 16.45″ N, 16° 19' 54″ E, 267 m a.s.l). Additional regional O_3 background observations surrounding Vienna shown are located northwest (O3_nw; Irnfritz; N 48.7244 E 15.5003; rural), northeast (O3_ne; Mistelbach; N 48.57861 E 16.58056; suburban), southeast (O3_se; Himberg; N 48.08611 E 16.43333) and south: (O3_s; Wiesmath; N 47,6083 E 16,2931; rural).

Initially all data were averaged to hourly values. If not stated otherwise, for AT, daily maxima were used. For GR and PR, the daily sums were used, while for the WD the daily mean was used. The planetary boundary layer height (PBL) was obtained from the Austrian meteorological service (ZAMG) as hourly data. We use the daily maxima of PBL as they coincide with the daily maxima of AT.

The O_3 data were obtained from the European Environmental Agency (EEA) and are based on measurements performed by the Viennese environmental agency in the Vienna city centre (site Wien Stephansplatz; Fig. 1). For O_3 we use the maximum daily 8-h average (mda8).
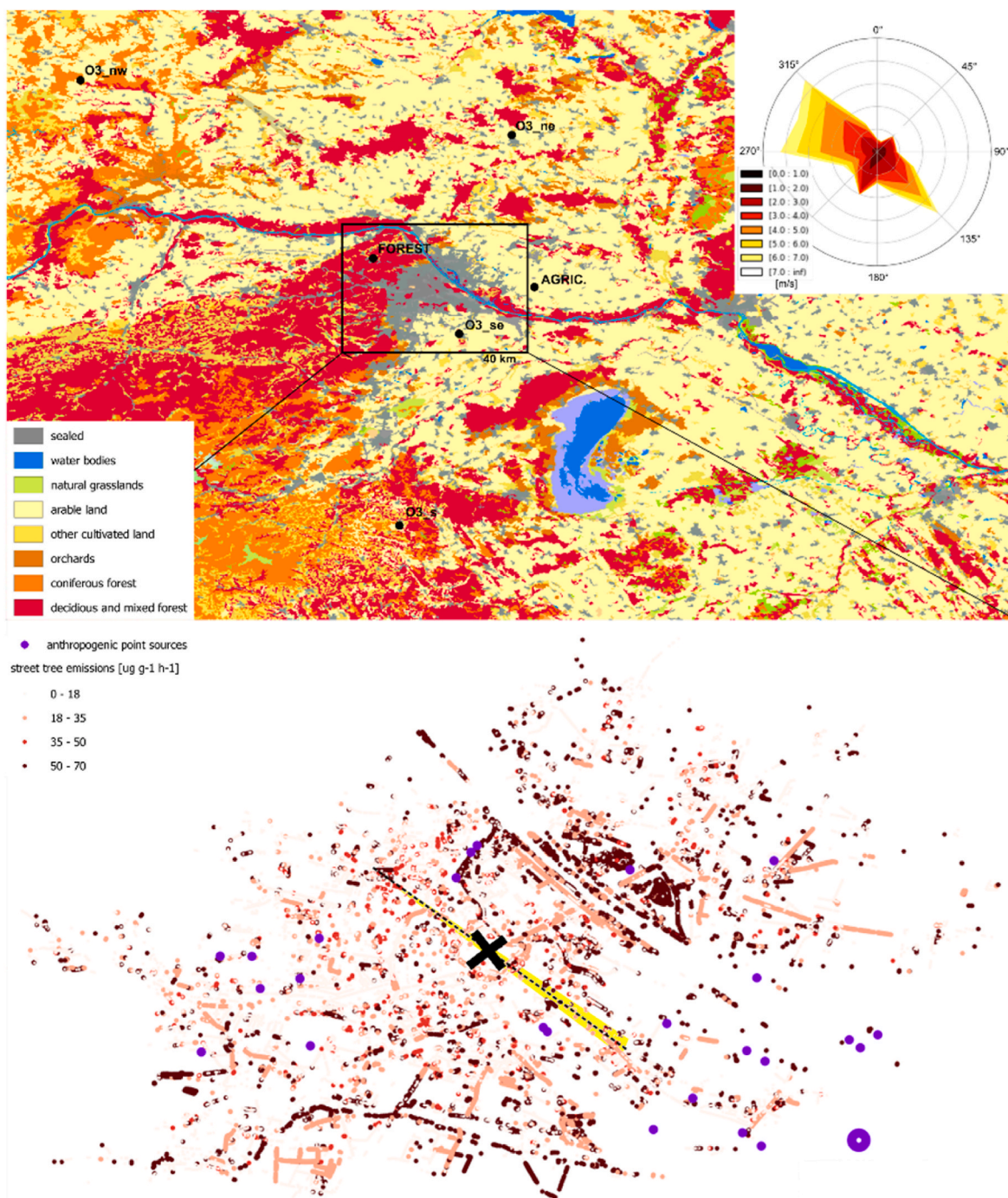
Fig. 1. Overview of the study region with landcover type according to Corine landcover 2006. Note, red and orange areas mark forests, which are potential HCHO precursor emission areas. The points used for relative soil saturation are marked with "AGRI". The centre point of the samples used for the satellite derived vegetation indices is marked with "FOREST". The wind rose refers to the wind direction measured in the Vienna inner city. The black rectangle marks the closeup region. Within this region small dots mark urban trees with substantial emission factors, while purple dots mark anthropogenic emission sources from energy and industry sector including a petroleum refinery (large purple dot). The black dotted line in the closeup shows the line of sight of the MAX-DOAS instrument at BOKU towards the southeast. The O_3 measurement site Wien Stephansplatz is marked with a black cross.

2.3. HCHO data

We use observed HCHO mixing ratios as a proxy for BVOC emissions. The HCHO data were obtained from measurements taken with the BOKU MAX-DOAS instrument within the VINDOBONA project (Schreier et al., 2020, http://www.doas-vindobona.at/) since 2017. This instrument is located at the BOKU platform and includes a spectrometer (Shamrock SR-193i-A), a CCD detector (ANDOR IDUS DV420A-BU), a telescope unit

mounted on a pan/tilt head, optical fibres, cables, and a measuring computer. Temperature control is configured for the spectrometer (+35 °C) and the detector (−35 °C), which are located inside the building. The BOKU instrument has an unblocked view towards the city centre. In this study, MAX-DOAS retrievals in the UV range with a spectral resolution of 0.5 nm, averaged over a light path in the azimuthal viewing direction 137° towards the city centre and air quality station Stephansplatz were used. The instrument has an opening angle of 0.8°

Table 1

Parameters analysed in this study for 2018–2020. (*) combination of products with spatial resolution of 500 m × 500 m; (**) fAPARa = Fraction of absorbed photo-synthetically active, radiation anomaly; (***) only measured during daylight.

Parameters	Acronym	Statistical value	Spatial Resolution	Source/Location
Global radiation	GR	Maxima	Point	BOKU
Air temperature	AT	Maxima	Point	BOKU
Wind direction	WD	Mean	Point	BOKU
Vapour pressure deficit	VDP	Mean	Point	Based on BOKU
Boundary layer height	PBL	Maxima	Point	ZAMG/Hohe Warte
Relative soil saturation	RSS	Mean	Point (*)	ARIS
Leaf area index	LAI	Sample	Satellite footprint	Proba V 300 m
Solar induced chlorophyll fluorescence	SIF	Sample	Satellite footprint	TROPOMI, OCO-2
fAPARa (**)	fAPARa	Sample	Satellite footprint	EDO/MODIS (MOD15a2H)
Standardized precipitation index	SPI	Sample	Satellite footprint	EDO
Formaldehyde	HCHO	Max (***)	Horizontal path	VINDOBONA project
Ozone	O_3	mda8	Point	City of Vienna/ EEA

and its optical path length varies between 5 and 10 km covering the centre of Vienna. In this study we used an elevation angle of 1°. Typical integration times are 30–60s in the off-axis and zenith-sky modes, respectively. Further description of the measurement setup can be found in Schreier et al. (2020).

The HCHO data were retrieved at 336.5–359 nm in the UV using a polynomial degree of 6, wavelength calibration using the Solar atlas (Kurucz et al., 1984) and the Fraunhofer reference from the sequential zenith spectrum. The differential slant column densities were converted to path-averaged mixing ratios, which have been further used in this study. The data are only available for the daylight hours, and data for zenith angles larger than 75° were omitted as well as measurements from optical path lengths below the 0.1 and above the 0.9 quantile. If not stated otherwise, daily maxima based on hourly values are used.

2.4. Observation-based drought and vegetation indices

Since a key focus of our study is to understand how BVOCs emissions vary and contribute to the HCHO burden in the Vienna region under drought conditions, a crucial methodological step is the selection of adequate dry and reference periods. To characterize the different aspects of drought in this multi-species heterogenous region we use a combination of several indices and quantities. As a measure of precipitation drought conditions, we use the indirect climate-based standard precipitation index (SPI) which derives drought stress from precipitation deficit. As an observed proxy for root zone drought conditions from reduced plant available water we use the relative soil saturation (RSS) of a close by agricultural area from the Agro Risk Information System (ARIS) - a drought monitoring system. For direct leaf level drought conditions affecting stomatal function we use the vapour pressure deficit (VPD). As an index of the first and most responsive response to water deficiency at the leaf level – decreasing turgor and slowing down of cell growth (Larcher, 2003) – we use an index for the absolute leaf area available for biogenic emissions and stomatal uptake - the remotely sensed leaf area index (LAI). Further drought causes hormonal induced stomatal closure to reduce transpiration (Peron et al., 2021). Thereby the gas-exchange between plants and the atmosphere is reduced, which

affects CO_2 assimilation, emission of BVOCs as well as O_3 uptake (Larcher, 2003). Further, with reduced CO_2 admission, photosynthesis is inhibited (Peron et al., 2021). To identify these effects on photosynthesis we use solar-induced chlorophyll fluorescence (SIF) and the reduced incoming radiation used by the plant's photo system photosynthesis measured by the fraction of absorbed photosynthetically active radiation anomaly (fAPARa). Below we describe these indices in more detail.

2.4.1. Standardized precipitation index (SPI)

The Standardized Precipitation Index (SPI-n, European Drought Observatory, 2021a) is a statistical indicator, which compares the total precipitation received at a particular location during a n-month period with the long-term rainfall distribution for the same period at that location. To allow for a statistical comparison of wetter and drier climates, SPI is based on a transformation of the accumulated precipitation into a standard normal variable with zero mean and a variance equal to one. Thus, SPI results are given in units of standard deviation from the long-term mean of the standardized distribution. WMO highlighted the SPI as a key meteorological drought indicator (World Meteorological Organization, 2012). In this study we have chosen SPI-3 as index for cumulative soil moisture deficit. For spring SPI-3 includes the previous winter months, while for summer SPI-3 includes the previous spring. The SPI is used in this study to select the pairs of driest and wettest seasons during 2018–2020.

2.4.2. Relative Soil Saturation (RSS)

Within the ADA project (Agro Drought Austria, 2021) a daily operational drought monitoring and forecasting system (ARIS) was developed for the main agricultural crops grown in Austria (winter wheat, summer barley, corn, sugar beet and grassland) using different indicators. For ARIS the meteorological data are obtained from the Integrated Nowcasting through Comprehensive Analysis (INCA) data set (Haiden et al., 2011). ARIS uses further soil data from the digital soil map of Austria (eBOD; BFW, 2021a) and land cover information from CORINE (Copernicus, 2021). ARIS products are calculated for two soil depths (0–40 cm and 40–100 cm for agricultural crops, 0–20 cm and 20–40 cm for grassland).

RSS is a key output from ARIS, and we use this daily index in addition to SPI to gain information on soil moisture deficits on shorter time scales, which may lead to delayed or reduced leaf deployment and reduced BVOC emissions. Unfortunately, no RSS is available for forested regions, thus we use the lower level of RSS for winter wheat (_w) and grass (_g) to illustrate the bandwidth of ambient soil moisture conditions. Specifically, we use RSS from the Rutzendorf site, a monitoring site representative for soil conditions in the study area (Fig. 1, "AGRIC."). For convenient reference we provide maps of regional soil type and clay fraction from eBOD in Supplemental Figs. S1 and S2.

2.4.3. Vapour pressure deficit (VPD)

We include VPD as an indicator for plant drought stress, given that vegetation stress does not necessarily depend only on soil moisture conditions. VPD directly influences the stomatal function on a specific day (Stoy et al., 2021). VPD was calculated via saturated vapour pressure (e_sat) from hourly mean air temperature (T) and relative humidity (RH) following Dingman (2002): VDP = e_sat – (RH*e_sat/100), with e_sat = 0.611 * exp((17.3*T)/(T+237.3)).

2.4.4. Leaf area index (LAI)

The dimensionless LAI is commonly used to characterize the canopy of an ecosystem (Bréda, 2003), which was defined by Watson (1947) as the total one-sided area of leaf tissue per unit ground surface area. In this study, we use the Project for On-Board Autonomy - Vegetation PROBA-V; (Sterckx et al., 2014) LAI product CGLS_LAI300_V1_GLOBAL (Fuster et al., 2020) with a 300 m spatial resolution and a temporal resolution of one day, as available from the Copernicus Global Land Service (CGLS). Specifically, we extract values over the forest areas west

of Vienna (for an approximate 12 × 11 km domain; 48.22 N–48.32 N, 16.1 E – 16.26 E) and use the domain average LAI as proxy for biomass in this study.

2.4.5. Solar-induced chlorophyll fluorescence (SIF)

Chlorophyll fluorescence is a direct indicator of the vitality of the plant photosynthetic apparatus, and a reduction of SIF indicates stress causing a reduction of photosynthesis (Meroni et al., 2009). SIF has a quasi-linear relationship with ecosystem photosynthesis (gross primary productivity - GPP), especially for larger spatial and temporal scales (Fu et al., 2021). Thus, we use SIF as one of two indices to detect drought effects on photosynthesis. SIF can be derived from ground, airborne and spaceborne measurements of different instruments. In this study we use the TROPOMI and the OCO-2 SIF data sets (Bacour et al., 2019a, 2019b; Guanter et al., 2015; Köhler et al., 2018). Given that the TROPOSIF_L2B product (SIF_743) is only available from May 2018, we supplement this record by OCO-2 SIF data between January and April 2018. Both the TROPOMI SIF and OCO-2 SIF retrievals were extracted for a central point in the forested region (48.28° N, 16.23° E; Fig. 1, "FOREST").

2.4.6. Fraction of absorbed photosynthetically active radiation anomaly (fAPARa)

As a second index for the detection of drought effects on photosynthesis we use fAPARa. The fAPARa product is provided by the European Drought Observatory (European Drought Observatory, 2021b) for 10-day consecutive periods with a spatial resolution of about 4 km. This product is computed from the MOD15A2H release, which is calculated using a three-dimensional radiative transfer model in which the atmospherically corrected reflectance obtained by MODIS and a global biome map are used (Yan et al., 2016a, 2016b). The fAPARa used in this study was extracted for the same grid point as SIF (Fig. 1, "FOREST").

2.5. Numerical models

We use three types of numerical model in this study and each has a specific purpose. 1) To supplement the observation-based drought indices (described in Sect. 2.4) we use a land surface model (Section 2.5.1 SURFEX) to track the evolution of the drought and heat wave effects and to provide dynamic simulation of vegetation and soil moisture response. 2) We use a bottom-up BVOC emission model (Sections 2.5.2 and 2.5.3 MEGAN) coupled to the land surface model outputs and meteorological data to estimate BVOC emissions. 3) Finally, we use a chemical transport model (Sect. 2.5.4 MOCAGE) run with the MEGAN BVOC emissions in order to estimate the impacts the heat wave and drought have on BVOC emissions and in turn to estimate the resulting HCHO atmospheric concentrations.

2.5.1. SURFEX

The SURFEX (SURface EXternalisée) land surface model (Masson et al., 2013) simulates heat, moisture, and gas fluxes at the atmosphere-surface boundary and is designed to be coupled with meteorological models and atmospheric forcing both online and offline, respectively. SURFEX simulates Earth's surface by splitting its surface into four broad types: nature, town, fresh water (lakes, rivers, and lagoons), and sea. Nature forms the broadest land surface type as it includes all natural and cultivated, and all vegetated and all non-vegetated land surface types. Nature, consequently, is broken down into sub classes representing different types of biomes and agricultural land use. The ISBA-A-gs scheme (Calvet et al., 1998) is used to simulate all land surface classes within the nature type. SURFEX is used in a wide range of applications, e.g., river discharge prediction (Fairbairn et al., 2017), drought monitoring (Albergel et al., 2019), and urban climate studies (Schoetter et al., 2020). SURFEX can be configured to dynamically simulate changes in vegetation according to how meteorology impacts the growing season, which results in a dynamic representation of LAI. The use of this dynamic representation of vegetation has shown to be

skillful at reproducing phenological changes and soil moisture on seasonal timescales when forced with state-of-the-art meteorological atmospheric forcing (Albergel et al., 2019).

SURFEX can also perform data assimilation of satellite observations of land surface variables (soil moisture and LAI) using the Extended Kalman Filter (Albergel et al., 2017). This configuration using data assimilation is termed SURFEX LDAS-Monde (Land Data Assimilation System-World/Global). Assimilation of satellite observations of LAI in SURFEX LDAS-Monde has been shown to improve estimates of the soil moisture content and of phenological changes (Albergel et al., 2017).

In this current study of Vienna, we assimilate the PROBA-V LAI satellite observations (Verger et al., 2014) to improve the estimation of the vegetation state (see Section 2.4.4). SURFEX was run over the full year of 2019 at a spatial resolution of 0.1° × 0.1° offline, covering a spatial domain matching the current Copernicus Atmospheric Monitoring Service regional domain (Marecal et al., 2015), and was forced by ECMWF HRES meteorological data at this resolution. SURFEX was run using the ECOCLIMAP-2 land cover map (Faroux et al., 2013). This simulation was run using SURFEXv8.1. SURFEX run with the nitrogen dilution photosynthesis option on. This option includes a drought response of vegetation and evolves Leaf Area Index according to calculations of photosynthesis for above-ground biomass calculated with nitrogen dilution for herbaceous vegetation and forests (Calvet et al., 2004; Calvet and Noilhan, 2000).

The LAI and soil moisture output from SURFEX is used as input to MEGAN3 (in an offline configuration, Sect. 2.5.2) (Guenther et al., 2020) and MEGAN2.1 (in an online-coupled configuration, Sect. 2.5.3) (Guenther et al., 2012).

2.5.2. SURFEX-MEGAN3

We have developed a coupling setup between the SURFEX land surface model and the MEGAN3 BVOC emission model, which from now on we term SURFEX-MEGAN3. The SURFEX-MEGAN3 has been continued and run within the SEEDS in the European CAMS domain for 2019 using the SURFEX land surface model outputs for root zone soil moisture (5th soil layer down) and LAI (Section 2.5.1) based both a free-running model (termed open-loop) and that using the LAI assimilation. The coupling between the land-surface model SURFEX and MEGAN3 significantly improves the soil moisture and leaf area index information that is used within MEGAN3 to calculate BVOC emissions. MEGAN3 calculates the emission factors using the MEGAN3-EFP python code that is provided with the main MEGAN3 fortran code. MEGAN3 introduces updated emission factors and algorithms based on recent measurements, treatment for processes unrepresented in MEGAN2.1 including stress induced emissions and canopy heterogeneity. This improvement propagates to precision of the MEGAN3 isoprene emissions. Both isoprene and formaldehyde are part of the 19 biologically lumped emission species calculated by MEGAN, which is converted directly to one of the 38 chemically lumped species of the RACM mechanism (Stockwell et al., 1997).

2.5.3. SURFEX-MEGAN2.1

We also use an alternative coupling setup between SURFEX and MEGAN. The land surface model SURFEX was coupled online to the BVOC emission model MEGAN2.1. This online coupling means that the MEGAN2.1 model is embedded within SURFEX and it is executed when SURFEX is run. Similarly, to before, the motivation for this coupling was to try to improve the BVOCs flux estimation by using the ISBA scheme included in SURFEX to provide more precise, vegetation-type dependent input parameters (LAI and soil moisture) to MEGAN2.1.

In the coupled model, the estimation of the biogenic flux is done by using vegetation types extracted from ECOCLIMAP-II, which is a 1-km global database of land covers made by CNRM (Centre Nationale des Recherches Météorologiques) (Masson et al., 2003). ECOCLIMAP-II includes a description of 19 vegetation types also called patches in addition to land parameters associated to each type of vegetation: 3 soil

depths (root, soil, ice), height of trees and LAI (Leaf area index) available at 10 days' time step. A mapping was done in order to associate to each patch defined in ECOCLIMAP-II its corresponding vegetation type in CLM4.

MEGAN uses the same meteorological driving variables used as input to SURFEX (temperature, precipitation rate, incident shortwave radiation, CO_2 concentration and wind speed). The incoming PAR at the top of the canopy was assumed to be 48% of the incoming shortwave radiation. SURFEX-MEGAN2.1 uses a different approach to the vegetation parameters as compared to SURFEX-MEGAN3. In this case, the LAI is extracted from the ECOCLIMAP-II database for each vegetation type independently. As before, SURFEX-MEGAN2.1 uses the soil moisture of the 5th soil layer (corresponding to the root zone) and uses the wilting point calculated from the fraction of sand and clay to estimate the soil moisture activity factor. SURFEX-MEGAN2.1 uses ECOCLIMAP-II to estimate the emission potential map for isoprene (this map was provided with the MEGAN code).

2.5.4. MOCAGE

The MOCAGE model (MOdèle de Chimie A Grande Echelle) is a three-dimensional chemistry-transport model (CTM) for the troposphere and stratosphere (Guth et al., 2016; Lamotte et al., 2021) that simulates the interactions between physical and chemical processes. It uses a semi-Lagrangian advection scheme (Josse et al., 2004) to transport chemical species. It has 47 hybrid levels from the surface to 5 hPa with a resolution of about 150 m in the lower troposphere increasing to 800 m in the upper troposphere. Turbulent diffusion is calculated with the scheme of Louis (1979) and convective processes with the scheme of Bechtold et al. Its chemical scheme is RACMOBUS. It is a fusion of the stratospheric scheme REPROBUS (Lefevre et al., 1994) and the tropospheric scheme RACM (Stockwell et al., 1997). It includes 119 individual species with 89 prognostic variables and 372 chemical reactions. This gives MOCAGE the flexibility to be used for stratospheric (El Amraoui et al., 2008) and tropospheric studies (Dufour et al., 2005). It is also used in the operational air quality monitoring system in France: Prev'air (Honoré et al., 2008) and in the European forecasting service CAMS. A detailed validation of the model was done using a large number of measurements during the ICARTT/ITOP (Intercontinental Transport of Ozone and Precursors) campaign (Bousserez et al., 2007). In its basic configuration, used in this study, the model uses a $1° \times 1°$ global domain, forced by ARPEGE meteorological forecasts and fed by MACCity emissions representative of the year 2016, as well as a regional zoom over Europe (28 N–72 N, 26 W to 46 E, 0.1° resolution) driven by IFS and fed by CAMS-REG-APv4.2 emissions representative of 2018.

2.6. Periods of investigation

Given limitations in the availability of long-term HCHO data our analysis focuses on the years 2018–2020, which includes distinct dry and regular moister conditions. As we are interested in characterizing the influence of dry vs. wet conditions on BVOC emission and their contribution to ambient O_3 burden during the vegetation season we select from the data available the driest and wettest spring (MAM) and summer (JJA) seasons based on meteorological drought characterized by SPI-3 (Supplement Fig. S3). This selection yielded spring 2020 (MAM20) and summer 2019 (JJA19) as the driest spring and summer, respectively. Spring 2018 (MAM18) and summer 2020 (JJA20) were selected as the reference wettest spring and wettest summer seasons, respectively, based on recorded precipitation and soil moisture. The calculation of the days, falling below the air stagnation index (ASI) threshold (<3.2 ms^{-1} surface wind, <13ms^{-1} 500 mbar wind and no precipitation) shows that for the selected seasons (MAM18 and MAM20; JJA19 and JJA20) similar amounts of stagnation days took place (Table 2). For the spring seasons the ASI threshold days are very similar but the boundary layer height is higher in MAM20 (the dry spring) (+17%). For the summer seasons the boundary layer height is very

similar but there are 25% more days exceeding the ASI threshold in JJA2019 (the dry summer) compared to the reference season.

3. Results

We perform a comprehensive analysis of the datasets introduced in Section 2.2 to 2.4 for the period 2018 to 2020. First, in Section 3.1 we show the timeseries of the analysed variables to illustrate the broad seasonal correlation of the abundance of O_3 and HCHO with meteorological, hydrological and vegetation parameters. In Section 3.2 we investigate the changes in HCHO mixing ratios as a response to environmental parameters. In Section 3.3 we focus on the influence of flow direction and anthropogenic influences. Section 3.4 focuses on the vegetation and meteorological conditions that occurred during periods with elevated ozone concentrations. Finally, Section 3.5 is focused on the study of the impacts of the 2019 summer drought on simulated isoprene emissions and HCHO.

3.1. Timeseries analysis

Before we present detailed results of our analysis, we set the scene and refer the reader to Fig. 2, which shows the most relevant parameters for the full period of the study. Here we highlight two spring seasons (orange shading) and two summer seasons (red shading), which are discussed in detail below. Fig. 2a shows that O_3 (magenta) and GR (yellow) correlate well during spring and summer 2018 (R = 0.69) and 2019 (R = 0.65), but during the spring and summer of 2020 this relation stops (R = 0.47) as much lower O_3 concentrations emerged compared to previous years while GR remained at similar levels, which motivates our analysis in Section 3.4 below. Fig. 2b introduces the vegetation related variables, which follow the same annual pattern. Here we show in green the LAI whose smooth values are due to the averaging process of high-resolution footprint pixels. For SIF we show the values of two satellite platforms which agree well in the region of overlap, but whose absolute values indicate an uncertainty of about 30%. Fig. 2c shows the daily PR sums and the RSS for wheat and grassland as soil moisture information. Note, the change in RSS following larger precipitation events. Finally, we illustrate in Fig. 2d the relationship between HCHO concentrations and VDP, which strongly covary (R = 0.75 for the full period).

We focus on the periods of particular interest in Figs. 3 and 4, which focus on spring (2018 and 2020) and summer (2019 and 2020), respectively. Looking first at spring, we see that while radiation evolved similarly in MAM18 and MAM20, vast reductions emerged in MAM20 O_3 levels compared to those of MAM18 (Fig. 3a). Given that O_3 formation at the investigated site is VOC limited (Mayer et al., 2022), we hypothesize that the reduction in O_3 levels may stem from reduced BVOC amounts. Fig. 3b illustrates that after a strong positive fAPAR anomaly at the beginning of the MAM20 season, a pronounced negative fAPARa anomaly occurred, indicating vegetation stress during the latter stages of MAM20 compared to MAM18, likely resulting from reduced soil water content (Fig. 3c). Note that precipitation during May 2020 did not suffice to compensate for the extensive dry spell during previous months leading to a relatively fast reduction of RSS (Fig. 3c). The decline in fAPAR coincides with the increase of soil moisture deficit (Fig. 3c) and only lessens in severity after about 20 days when the soil moisture starts to recover after precipitation events (Fig. 3b and c).

HCHO mixing ratios begin to differ strongly between MAM20 and MAM18 starting in April of both periods, which aligns with the differences in fAPARa and RSS (Fig. 3b and d) that arise throughout this period: RSS March 15 – May 25, and fAPARa May 10–31. The reduced HCHO mixing ratios during MAM20 compared to MAM18 provide support to our hypothesis that the cause of reduced O_3 formation is due to reduced BVOC emission. This is further strengthened when we consider that both AT and GR, which are the other important drivers of photochemical O_3 formation, are very similar during MAM18 and MAM20. An influence of reduced NO_x concentrations is excluded due to

Table 2

Comparison of average values of environmental parameters during the analysed seasons for NW days (AT: air temperature (°C), GR: global radiation (kWh/d/m^2), RSS: relative soil saturation of grass (_g) and winter wheat (_w), SIF: solar-induced chlorophyll fluorescence (mWm^{-2}sr^{-1}nm^{-1}), VPD: vapour pressure deficit (kPa), HCHO: formaldehyde (ppb), O$_3$ concentrations (µg/m^3), PBL: planetary boundary layer height (m), ASI: air stagnation index (days with threshold of daily surface wind below 3.2 m s-1, no precipitation and 500 hPa wind <13 m s-1 at 48.25 N 16.5 E from ERA5 data), WS: windspeed [m/s].

| NW, d	AT	GR	RSS_g	RSS_w	SIF	VPD	HCHO	O$_3$	PBL	ASI	WS
MAM18	12.25	3.7	0.77	0.72	0.46	0.85	0.93	83.7	1658	19	2.5
MAM20	14.12	4.6	0.56	0.50	0.81	0.92	0.71	79.5	1935	16	2.7
JJA19	24.67	5.9	0.21	0.02	1.19	1.68	1.83	101.1	1771	41	2.3
JJA20	22.49	5.0	0.04	0.01	1.42	1.28	1.46	80.7	1723	33	2.7
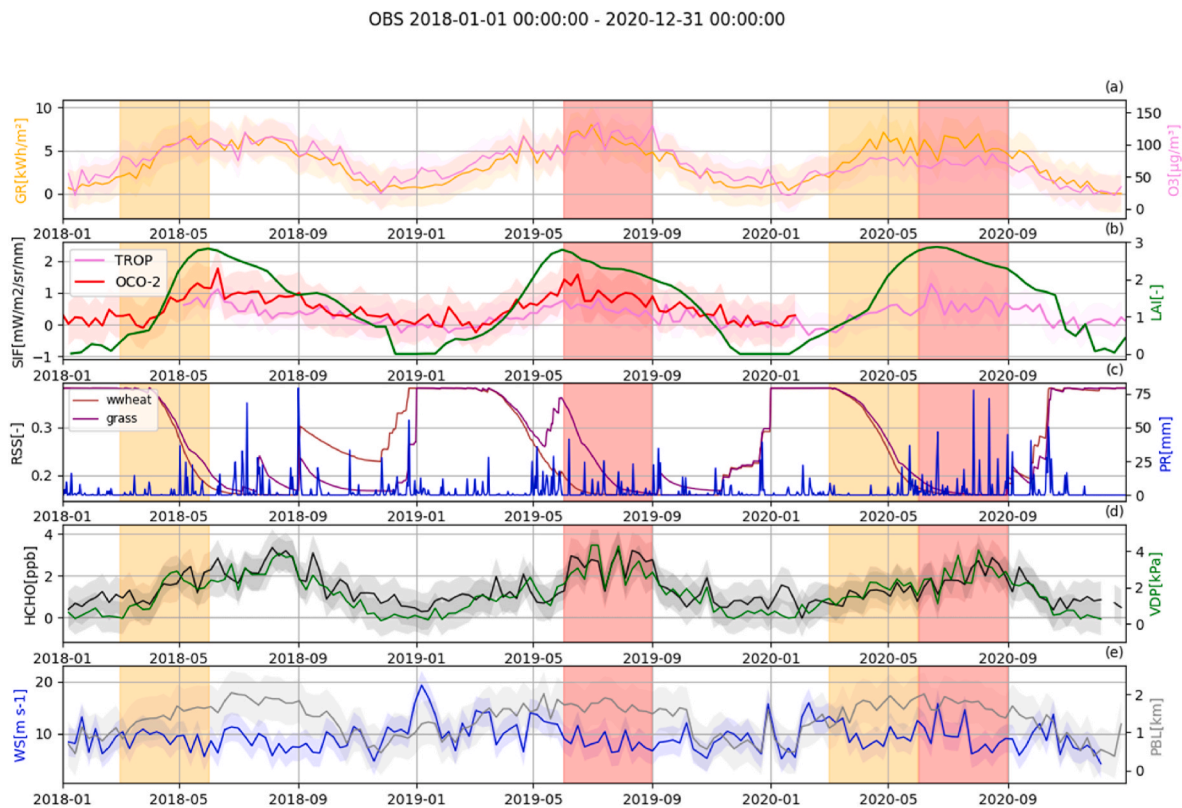
Fig. 2. Time series of (a) O$_3$ (purple) and GR (yellow), (b) SIF (red, purple), LAI (green) (c) RSS winter wheat (brown), RSS grass (violet), PR (blue), (d) HCHO (black), VPD (green), (e) WS (blue) and PBL (grey). Selected spring (MAM18, MAM20: orange) and summer (JJA19, JJA20: red) seasons are indicated by vertical shading across panels. For weekly average values (GR, O$_3$, SIF, HCHO, VDP, WS, PBL) the shading indicates the standard deviation of daily values during the full time period.

(1) VOC limitation of the chemical regime (Mayer et al., 2022) and (2) that reductions in NO$_x$ emissions have been widely limited to Mid-March to Mid-April 2020 in Austria (Staehle et al., 2022).

We now look at the land surface and BVOC emission model data for the MAM periods in order to provide additional support for our interpretation of the drought impact in MAM20. In Fig. 4 we examine the LAI (Fig. 4a) and root zone soil moisture (Fig. 4b) data from the SURFEX land surface model as well as isoprene emissions (Fig. 4c) calculated by SURFEX-MEGAN3 for model grid boxes to the west of Vienna that have forest cover: one box is located 5 km to the west of BOKU, and the other in the Wienerwald. SURFEX represents the drier root zone soil conditions during MAM20, which impacts on the simulated springtime growth of vegetation leading to lower LAI (Fig. 4a) in both boxes. We have confirmed that the reduced LAI and soil moisture lead to reduced isoprene emissions (Fig. 4c) estimated by SURFEX-MEGAN3 during this same period by studying the model diagnostics related to both input variables. In contrast, root zone soil moisture conditions are wetter during MAM18, which leads to a more normal onset of the growing season and higher levels of LAI as compared to MAM20. This leads to on

average higher isoprene emissions simulated by SURFEX-MEGAN3. These findings are therefore supportive of the hypothesis proposed to explain MAM18 versus MAM20 conditions, i.e., that drought conditions suppressed vegetation growth and BVOC emissions, which in turn led to lower observed HCHO and O$_3$ mixing ratios and concentrations, respectively.

We now discuss the selected summer periods JJA19 (hot and dry) and JJA20 (reference). Contrary to findings in the selected spring seasons, O$_3$ was elevated in the relatively hot and dry JJA19 compared to JJA20 (Fig. 5a) although GR evolved similarly. After early July, fAPARa was clearly lower during JJA19 compared to JJA20, and SIF also trends lower in JJA19 after mid-July (Fig. 5b) indicating less gas-exchange and photosynthetic activity than in JJA20 for these periods. Prior to that in June, both fAPARa and SIF are on average higher in JJA2019 than in JJA20. We find a similar picture regarding PR and RSS, whereby there was increased precipitation and soil moisture in June 2019 relative to June 2020 but then greatly decreased precipitation and soil moisture moving into July and August (Fig. 5c). This also goes in line with the higher observed LAI in June 2019 compared to June 2020 but then
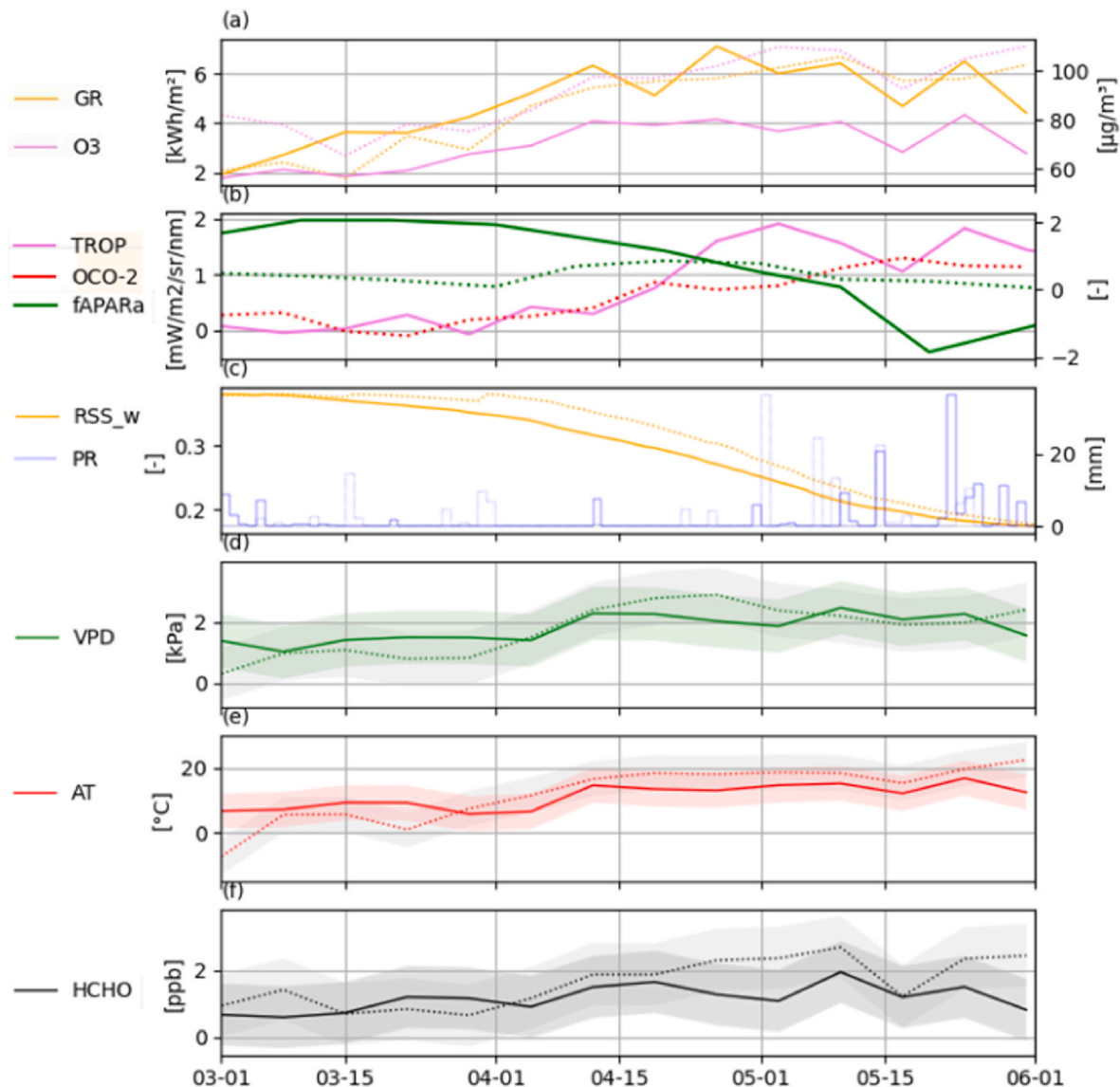
Fig. 3. Time series of weekly (a) O₃ (pink) and GR (orange), (b) SIF (TROPOMI: pink, OCO2: red), fAPARa (green) (c) RSS_w (orange), PR (blue), (d) VPD (green) (e) AT (red), (f) HCHO (black) comparing MAM20 (solid lines) to MAM18 (dotted lines). The shading in (d)–(f) shows the standard deviation of daily values.

lower LAI in the July and August of JJA19 compared to JJA20. VPD (Fig. 5d) and AT (Fig. 5e) on the other hand are higher throughout JJA19 compared to JJA20 especially at the beginning of the season (early June to mid-July 2019), which coincides with consistently higher daily average HCHO mixing ratios in JJA19 than in JJA20. We hypothesize that the phenological changes reflected by the reduced LAI in July–August 2019 presented in Fig. 2b, and the reduced SIF and fAPARa over the same period, are induced by the exceptionally warm AT and high VPD values occurring around mid and late June 2019. In other words, we hypothesize that these hot dry spells in June 2019 induce a drought, which is in turn represented by the changes seen in LAI, SIF, and fAPARa.

The JJA19/20 case, thus, presents a rather more complex picture than for the spring periods since there is some evidence of drought-driven phenological changes in the SIF, LAI, and fAPARa observations, but little apparent change in observed HCHO mixing ratios. For this reason, we now look at the land surface and BVOC model data from these JJA periods in order to look at the drought-driven processes in more detail. Fig. 6 looks at the SURFEX land surface model outputs of LAI and root zone soil moisture as well as the isoprene emissions from SURFEX-MEGAN3 for this period. Fig. 6b shows that root zone soil

moisture was higher in 2019 than in 2020 up until mid-June. There is some contrast of the Wienerwald site versus Schwarzenberg Park (close to BOKU), whereby the Schwarzenberg Park area actually reaches similar levels of dryness in 2019 as in 2020 by early-mid July. From early-July onwards in the 2019 simulation, LAI begins diverging between the selected grid boxes, which coincides with root zone soil moisture reaching critical levels in Schwarzenberg Park. Root zone soil moisture continues to decline even further in the Schwarzenberg Park grid box reaching the wilting point for these soil types whereas, despite some declines, it stabilizes at a higher level in Wienerwald. We see isoprene emissions in 2019 respond in contrasting ways at the Wienerwald and Schwarzenberg Park sites, but until early July when the declines in root zone soil moisture occur, isoprene emissions are relatively high at both sites and the peaks in emissions coincide with the hot periods in mid and late June. After early July, isoprene emissions at the Schwarzenberg Park site respond to the critical soil moisture levels and decrease to only nominal levels. The isoprene emissions at the Wienerwald site remain much higher even into mid-July during the warmer spells. Overall, the SURFEX model outputs of LAI and root zone soil moisture provide support for our stated hypothesis regarding drought- and heat-driven phenological changes in JJA19. The indication that the
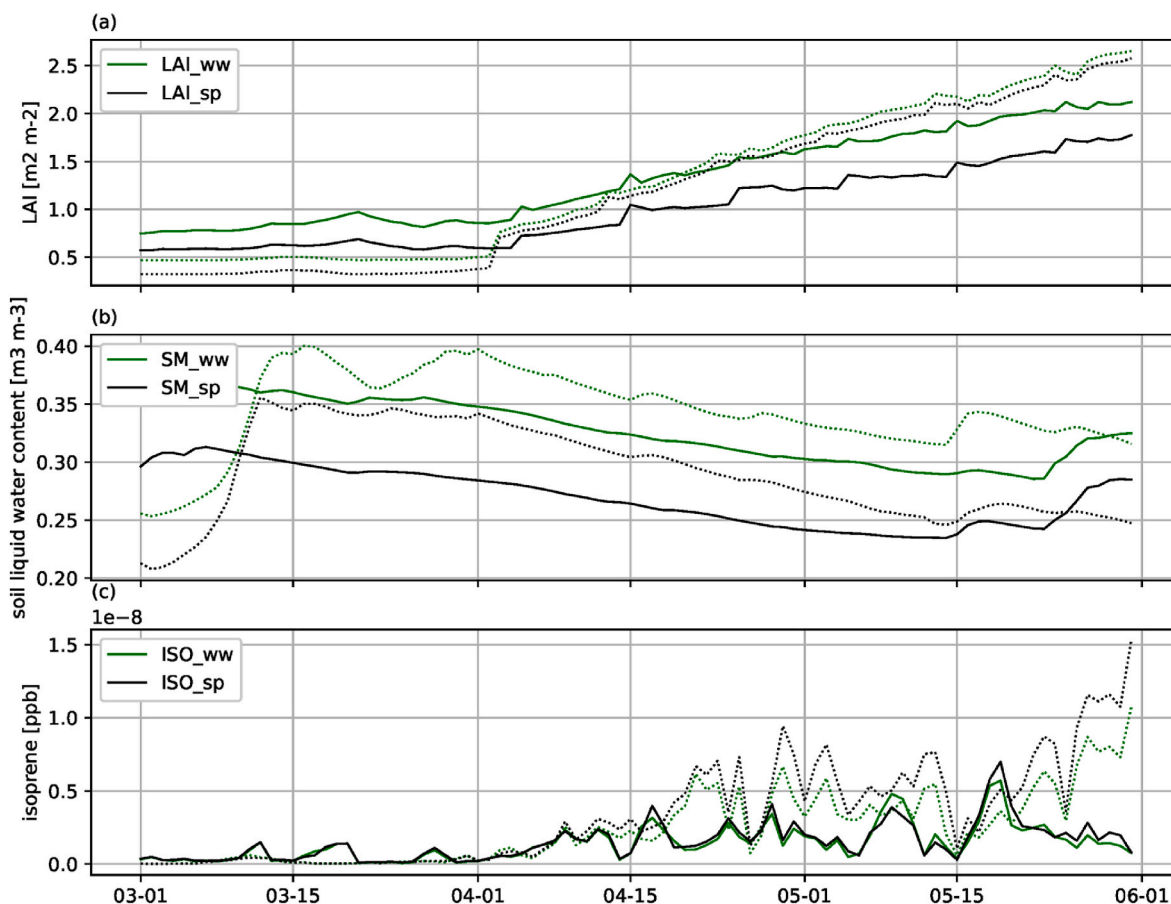
Fig. 4. Time series of daily SURFEX modelled (a) LAI and (b) root zone soil liquid water content, and isoprene emissions (c) from SURFEX-MEGAN3 (mean over UTC 08:00–14:00) for MAM20 (solid lines) and MAM18 (dotted lines). These data are shown for two forest areas: the first within the Wienerwald (labelled _ww/green lines at 48.04° N 15.95° E) and the second is in the area around Schwarzenberg Park (labelled _sp/black lines at 48.04° N 15.95° E).

drought induced sharp reductions in BVOC emissions in forests in close proximity west of the BOKU MAX-DOAS site (Schwarzenberg Park), yet not in forest areas in Wienerwald, makes drawing a causal link to the observed HCHO complicated. We, therefore, investigate this further in Section 3.3 by looking at the spatial evolution of the drought, and by analysing simulated HCHO mixing ratios from the MOCAGE model. However, the indication from SURFEX-MEGAN3 that BVOC emissions continue at Wienerwald even into mid-July gives tentative support to the idea that observed HCHO remain relatively high in July–August 2019 as a result of BVOC emissions from the forests surrounding Vienna that remain relatively unaffected by the regional drought.

3.2. Relation between HCHO and environmental parameters and its seasonal variations

Throughout each full year we find significant positive correlations between HCHO and AT, GR, SIF, VDP, O_3 and PBL, while we find significant negative correlation with RSS (Table S3). Generally, the correlation of HCHO with AT, O_3, RSS and VDP is stronger on days with O_3 mda8 values above 100 $\mu g/m^3$ and global radiation >4.5 kWh/day (Fig. 7, Table 3). Further within each year, the relation of the parameters towards HCHO changes. While the correlation between HCHO and AT is most pronounced during summer (due to larger emissions of BVOCs in the warm season and increased photochemical oxidation) it is weakest (and not significant) during the same season for HCHO and GR, not surprising as GR is high and not a limiting quantity for vegetation processes. The HCHO-RSS correlation is generally negative, thus under low soil moisture conditions more HCHO is present in the atmosphere. Conversely, SIF shows a positive correlation with HCHO, which means

the higher the vegetation activity the more HCHO can be found in the atmosphere. Here the strongest correlations are found during spring and autumn, which indicates that BVOC production is limited by vegetation activity during these seasons. O_3 shows a strong positive correlation with HCHO. The correlation is strongest in summer, not surprising given the importance of in-situ O_3 production over the impact of the background.

3.3. Anthropogenic contributions to HCHO mixing ratios

The relevant biogenic VOC sources are predominantly the large, forested areas surrounding the city of Vienna. Forest extent is particularly pronounced in the west (Fig. 1). On the other hand, anthropogenic sources of HCHO are predominantly located within the urban core (e.g., waste incinerators used for district heating), but also emissions from a refinery located southeast of Vienna are of importance. This refinery processes crude oil into fuel, various gases and bitumen and is known to emit 2% of the national anthropogenic VOC share per year. Furthermore, other smaller anthropogenic VOC emission sources are also located in the southeastern sector (Fig. 1). These include the Viennese oil port, which is connected to the nearby central tank farm and refinery.

Given the spatial separation of sources, we filter the available data based on wind flow direction. Our hypothesis is that larger HCHO mixing ratios occur during southeasterly flow when anthropogenic emissions add to the biogenic background. To test this hypothesis, we select from the time series clear sky days of mean wind direction from the southeast (SE; 90°–180°) or the northwest (NW; 270°–360°). Analyzing HCHO mixing ratios for these subsets illustrates that indeed higher HCHO mixing ratios are present on days with southeasterly
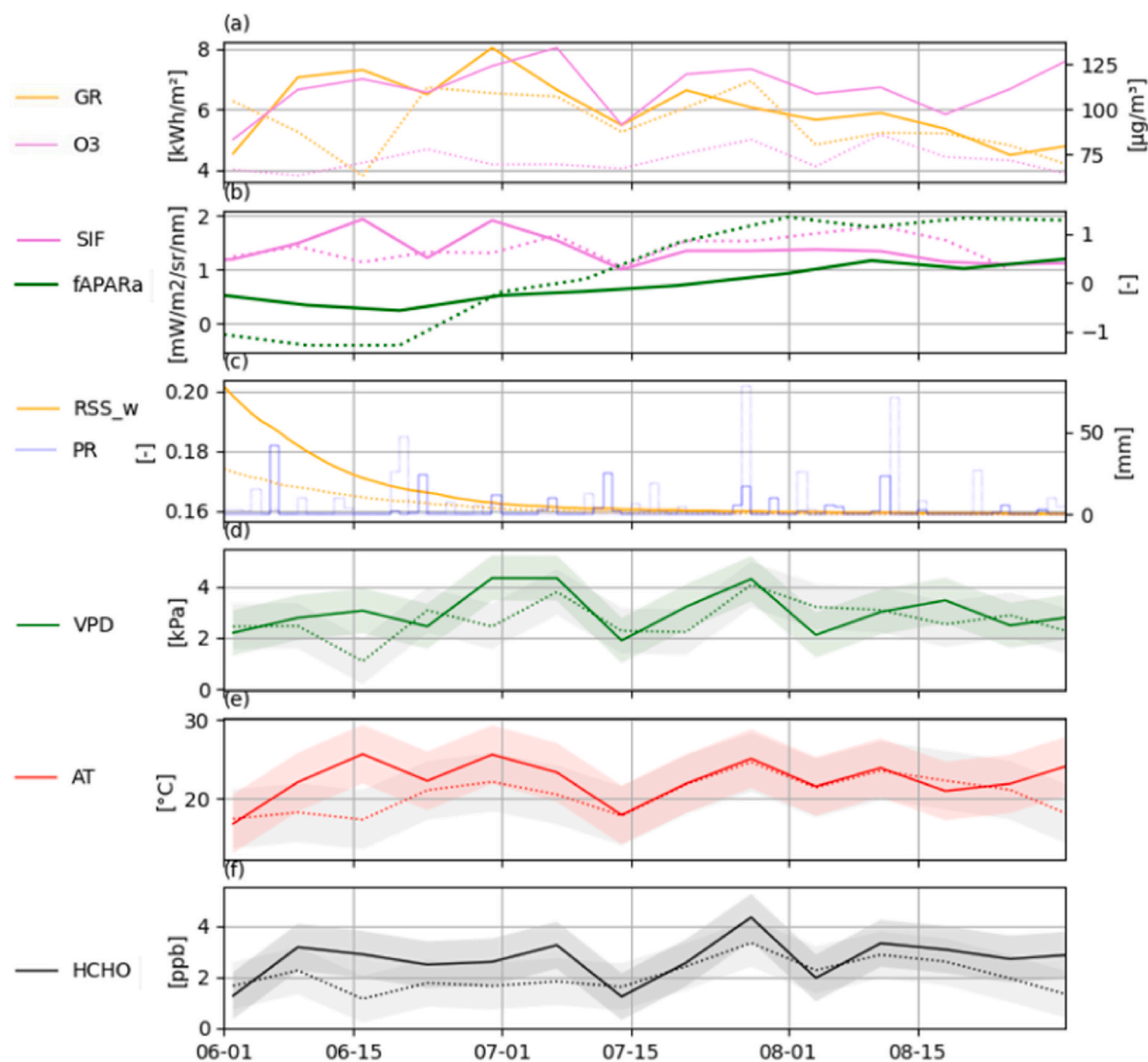
Fig. 5. Time series of weekly (a) O₃ (pink) and GR (orange), (b) SIF_TROPOMI (pink), fAPARa (green) (c) RSS_w (orange), PR (blue), (d) VPD (green) (e) AT (red), (f) HCHO (black) comparing JJA19 (solid lines) to JJA20 (dotted lines). The shading in (d)–(f) shows the standard deviation of daily values.

advection (see Fig. 8a). Southeasterly winds in Vienna are frequently associated with anti-cyclonic meteorological conditions that tend to bring warmer AT during the growing season. To confirm that this difference is indeed due to anthropogenic sources and not an artifact resulting from differences in AT (Fig. 8b), which could potentially drive both atmospheric oxidation of VOCs and BVOC emissions higher, we further investigate the statistical relationship between AT and HCHO for these subsets. To this end, a linear regression between AT and HCHO is established for the vegetated (VP; Apr–Oct) and non-vegetated (NVP; Nov–Mar) periods individually (see Fig. 8c). The HCHO-AT pairings are further separated in Fig. 8c according to wind direction, either northwest or southeast, in order to highlight potential differences in sources from both wind sectors. We estimate the contribution to observed HCHO mixing ratios of the anthropogenic sources in the sector to the southeast using a combination of the average difference in observed HCHO mixing ratios between the northwest and southeast sectors, the slope of the HCHO-AT plots, the correlation of each of the four HCHO-AT groupings, and the implied y-intercept of the HCHO-AT plots during the NVP. First, we look at the average differences in HCHO mixing ratios between the SE and NW subsets. The average differences in HCHO mixing ratio are 1.1 ppbv (VP) and 0.90 ppbv (NVP). We calculate corrections to the HCHO mixing ratios due to the temperature difference between the SE and NW subsets of 1.1 °C (VP) and 0.6 °C (NVP), and this yields changes

of 0.15 ppb and 0.02 ppb, respectively. Applying these changes to the VP and NVP HCHO mixing ratios indicates that 0.95 ppb and 0.88 are likely to originate from anthropogenic sources. The results yield a steeper slope for HCHO~AT during the VP (0.14 ppb °C-1) than for the NVP (0.04 ppb °C-1) (see Fig. 8c). Further, during the VP we find a higher Spearman correlation coefficient for the NW (0.92 compared to 0.76). During NVP the correlation coefficients from the NW and SE are very similar for both directions (0.46 compared to 0.43) on clear sky days. This indicates a higher dependence on of the NW data subset during the VP on the BVOC emissions. This dependence can also be seen in the lower spread of the residuals in the NW than in the SE (absolute mean error is 0.28 and 0.69, absolute variance of error is 0.05 and 0.55 for NW and SE, respectively). Finally, the anthropogenic influence in the SE also becomes clear during the NVP when we examine the implied y-intercept for the NW subset, which is lower (0.25 ppbv) compared to that for the SE grouping (0.81 ppbv). Thus, when no vegetation is present, for similar AT values, the HCHO levels are clearly higher for the SE grouping indicating higher non-natural sources.

3.4. Conditions during periods of elevated surface ozone concentration

The O₃ situation in the selected seasons is not a local but a regional matter as background stations around Vienna all fit well to the inner city
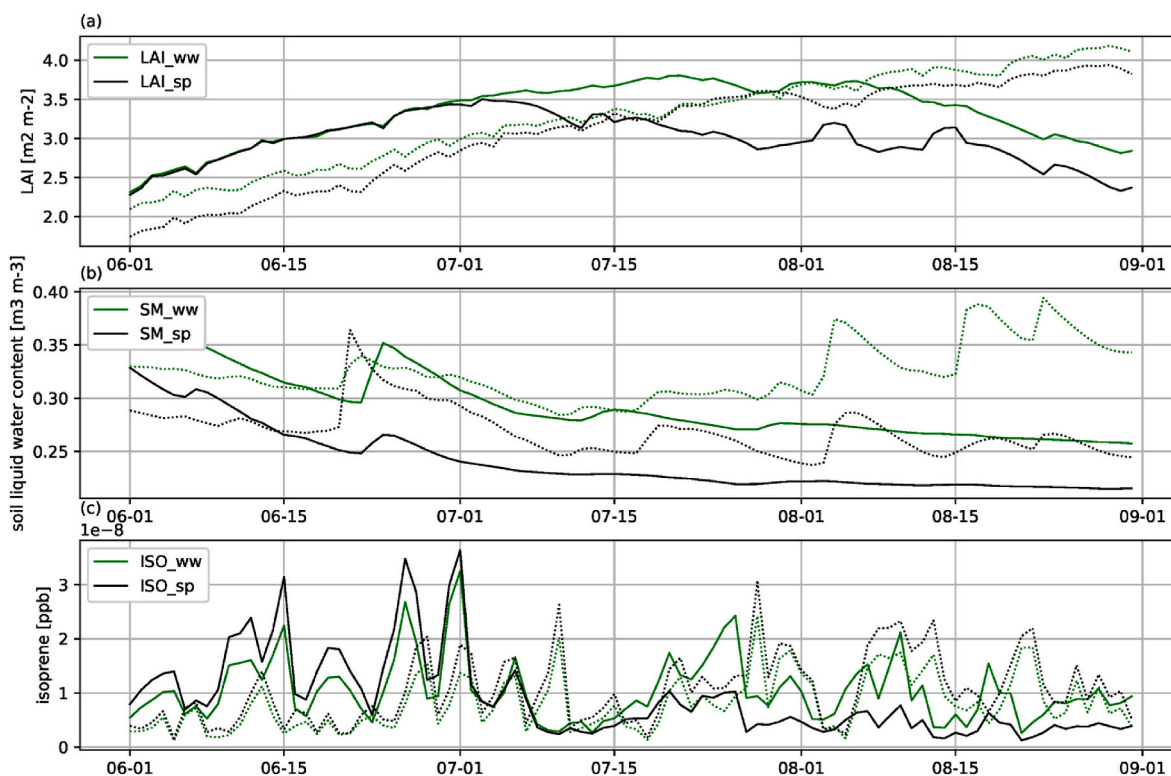
Fig. 6. Time series of daily SURFEX modelled (a) LAI and (b) root zone soil liquid water content, and isoprene emissions (c) from SURFEX-MEGAN3 (mean over UTC 08:00–14:00) for JJA19 (solid lines) and JJA20 (dotted lines). These data are shown for two forest areas: the first within the Wienerwald (labelled _ww/green lines at 48.04° N 15.95° E) and the second is in the area around Schwarzenberg Park (labelled _sp/black lines at 48.04° N 15.95° E).

station used for analysis (Fig. S4). Next, we focus on days with an elevated ozone burden. To this end we select days exceeding the mda8 100 μg/m^3 target value recommended by the WHO. For these days, the increased biogenic influence from the NW manifests in a more pronounced relationship between HCHO and AT, RSS, VPD and O$_3$ (Table 3). In comparison to days with airflow from SE, days with NW winds have lower absolute HCHO values but a stronger temperature dependence, which is an indication for the dominance of the biogenic source.

Next, we differentiate between dry and regular MAM and JJA seasons and analyse the role of ambient meteorological and environmental conditions for O$_3$ with a dedicated focus on NW flow. Compared to MAM18, MAM20 was characterized by higher GR, warmer AT and lower RSS during NW days (Table 2). Further, VPD was increased and fAPAR (0.45 to −0.42) and LAI (2.72–2.57) was reduced towards the end of MAM20 in May, which indicates plant stress (b,d). Consequently, both HCHO and O$_3$ have been lower under MAM20 conditions.

3.5. Simulated isoprene emission drought reaction and influence on HCHO

We now focus on summer 2019 and try to explain the somewhat conflicting findings of drought effects on simulated BVOC emissions and observed higher HCHO and O$_3$ during this period relative to JJA20. The results from the BVOC emission model SURFEX-MEGAN3 show that the isoprene emissions undergo a clear overall decline in the region close to Vienna (Fig. 9a–c) starting in July and into August 2019. This decline in isoprene emission corresponds to the onset of a drought represented in the simulated root zone soil moisture data in the regions around Vienna to the north, east and south (Fig. 9d–f). Other parameters such as fAPARa (Fig. 5b) and VDP (Fig. 5d) indicate, similarly, that also some plant stress occurred, which caused some limitation on additional BVOC release and potentially also on O$_3$ dry deposition. Other indicators for

plant stress might be the decrease in LAI (2.36–2.12, Figs. 3, Figure 6a) and SIF (1.59–1.15, Fig. 5b) during the last month of the season (Figs. 3). Notably, however, specific regions of forest to the immediate west-southwest of Vienna and further afield to the southeast of the city remain less affected by the drought and maintain moderate levels of isoprene emissions even in July and August. We show a more detailed daily time series (Fig. 10) of the isoprene emissions at selected locations within the region to highlight this contrast in drought effects. We can see from this, that the forest regions in Wienerwald, the Leitha mountains, and around Lake Neusiedler maintain moderate to high levels of isoprene emissions (1.4–3.4 mol m^{-2} s^{-1}) during the hottest days in July (20th-25th) that had the highest observed HCHO and O$_3$ that month. In contrast, the locations Lobau and Schwarzenberg Park show greatly reduced isoprene emissions over this same period later in July as each of these locations lies within the region most affected by the low root zone soil moisture conditions that develop during July, i.e., <0.2 m^3 m^{-3}. The results from SURFEX-MEGAN3 are broadly consistent with those from SURFEX-MEGAN2.1 (see Fig. S6) for these same five locations. SURFEX-MEGAN2.1 reproduces the decline in isoprene emissions from that occurred in July 2019 in all locations, and that the decline was stronger in some locations compared to others. The differences between the different locations arises due to spatial variations in the emission factors used in MEGAN2.1 (calculated from ECOCLIMAP-II plant functional type maps) and MEGAN3 (calculated using the MEGAN3-EFP python code).

Next, we try to evaluate the impact these changes in emissions have on HCHO mixing ratios by using results from the MOCAGE chemical transport model. MOCAGE was run with the SURFEX-MEGAN3 BVOC emissions and, therefore, serves as a means to relate the simulated drought effects on isoprene emissions to simulated HCHO mixing ratios. Then by comparing the observed HCHO mixing ratios to those simulated by MOCAGE we have a means to evaluate whether the model captures the drought effects combined with any meteorological (radiation and
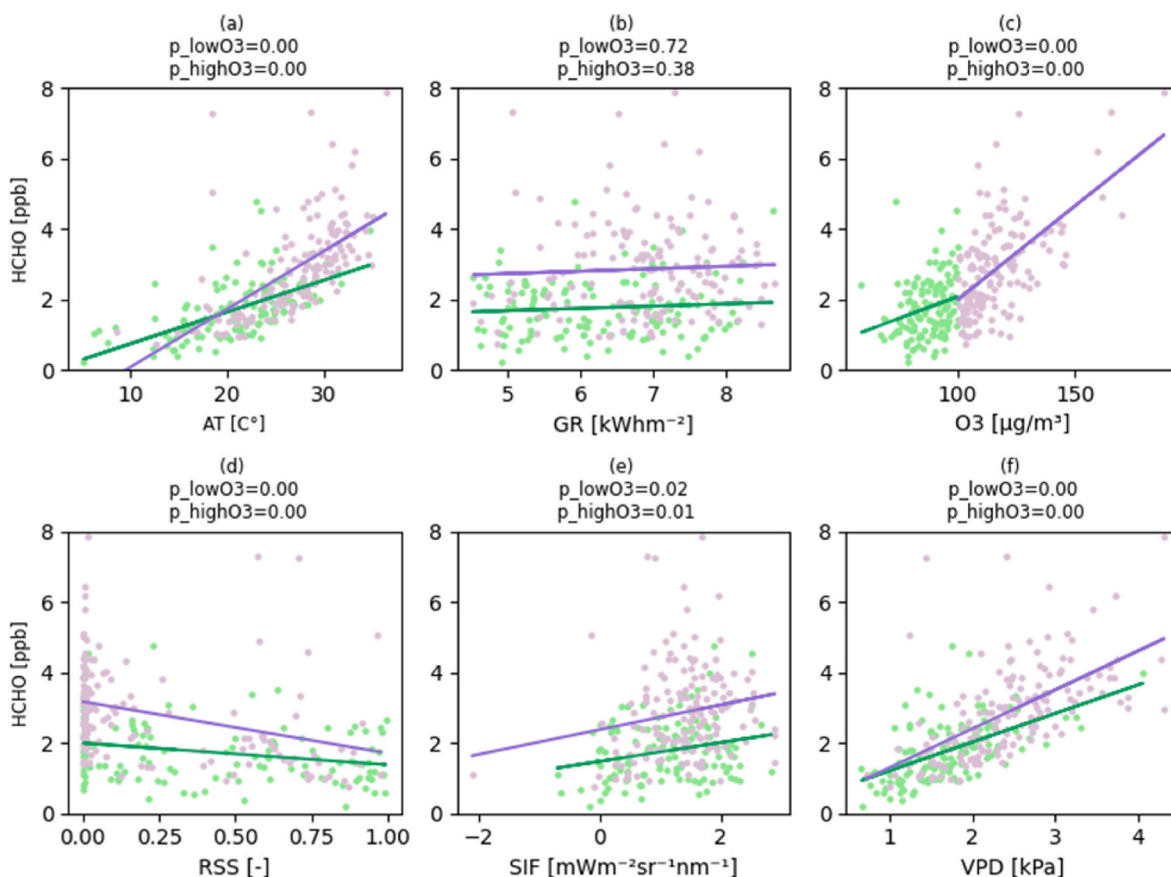
Fig. 7. Relationship between the measured daily maximum HCHO mixing ratios and (a) air temperature (AT), (b) daily global radiation sums (GR), (c) the daily mean mda8 concentrations (O_3), (d) daily mean relative soil saturation of winter wheat (RSS), (e) the daily mean solar-induced chlorophyll fluorescence (SIF), (f) the vapour pressure deficit (VDP), on clear sky days. Days with mda8 O_3 below the WHO O_3 threshold (lowO3) are shown in green, days above the WHO O_3 threshold (highO3) in purple. p-values of the Spearman correlation coefficients for lowO3 and highO3 samples are given on top of individual panels.

Table 3
Spearman correlation coefficient of HCHO with air temperature (AT), global radiation (GR), relative soil saturation (RSS) of grass (_g) and winter wheat (_w), solar-induced chlorophyll fluorescence (SIF), vapour pressure deficit (VPD), O_3 concentrations, and planetary boundary layer height (PBL) on clear sky days in 2018–2020, p-values >0.05 are given in grey italic font.

| Daily	AT	GR	RSS_g	RSS_w	SIF	VDP	O3	PBL
<100 µg/m³	0.67	*0.03*	−0.32	−0.26	0.20	0.60	0.29	−0.23
>100 µg/m³	0.73	*0.07*	−0.38	−0.43	0.21	0.69	0.55	*−0.09*
>100 µg/m³ SE	0.67	*−0.02*	−0.39	−0.42	*0.20*	0.65	0.46	*−0.03*
>100 µg/m³ NW	0.92	*0.08*	−0.42	−0.53	*0.02*	0.83	0.65	*0.27*

temperature) effects. The declining trend in isoprene emissions from June to August 2019 visible in Fig. 9 is reflected in Fig. 11d–f as a decreasing gradient of the HCHO-isoprene emission scatter over this period. This decreasing gradient represents a divergence between the simulated isoprene emissions at the forest site close to BOKU and the observed HCHO. If this local source were assumed to play a decisive role in affecting the observed HCHO this divergence could imply an erroneous prediction in decreased isoprene emissions as a result of the drought response. However, Fig. 11a–c shows that there is no noticeable divergence between the observed and modelled HCHO despite drought conditions reducing the simulated BVOC emissions in some forest regions (Lobau and Schwarzenberg Park). This implies that the forest regions (Leitha, Wienerwald, and Lake Neusiedler) that are unaffected by the drought continue to play an important role in contributing BVOCs that contribute to the observed HCHO.

Analysing the wind speed and direction in Fig. 11a–c to help assess source region we see that during June the days with high observed HCHO can be found for all wind speeds and directions, which indicates

strong contributions from local sources. However, during July and August the highest measured (>3 ppb) and modelled HCHO levels occur when the wind speed is lowest and when the air flow is from the southeast. These days in July and August with the highest observed HCHO coinciding with light winds from the southeast are associated with hot dry anticyclonic conditions. As we highlighted in Section 3.3, southeasterly winds typically lead to an anthropogenic contribution to the observed HCHO at the site in Vienna of 0.95 ppbv during the growing season. Overall, this implies that a combination of favourable meteorological conditions (elevated air temperatures and radiation), BVOC emissions from the forest areas less impacted by drought, and the anthropogenic sources to the southeast of the city contribute to the highest observed HCHO in July and August.

All described models MEGAN emission models (SURFEX-MEGAN2.1 and SURFEX-MEGAN3 open-loop and LAI analysis) have been compared to the observed HCHO in Vienna, show a very similar reaction to meteorology, and have a Spearman correlation coefficient of above around 0.7 (0.70/0.68/0.74; Fig. S6 Annex) between modelled isoprene
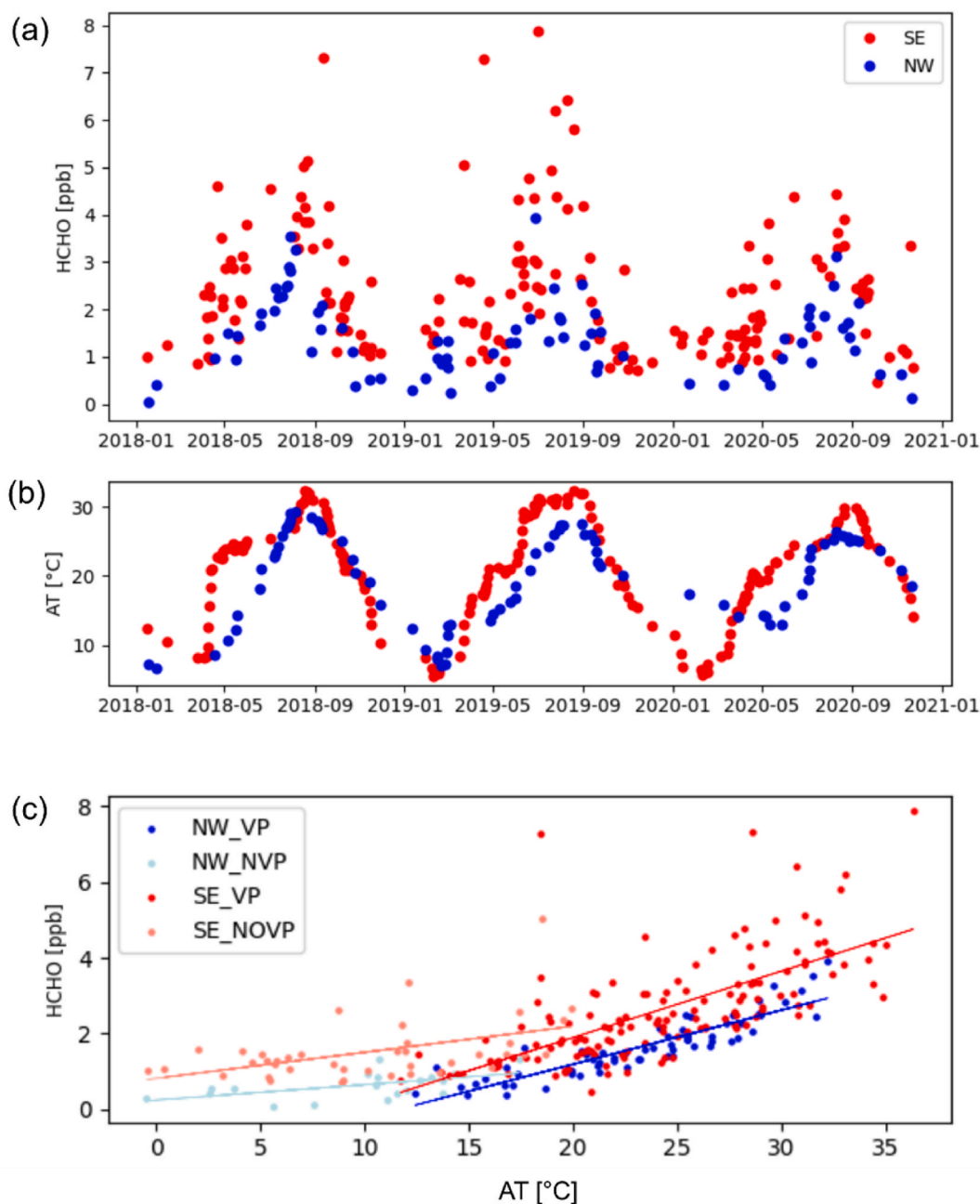
Fig. 8. Temporal evolution of the clear sky 7-day mean of maximum (a) volumetric mixing ratios of HCHO and (b) air temperature (AT) with mean wind direction from Southeast and Northwest. (c) relationship between HCHO and AT for clear sky days during vegetation (VP) and non-vegetation (NVP) season for air flow from Northwest and Southeast (color coded).

and observed HCHO. Lastly, we hypothesize, therefore, that without the vegetation stress incurred on some forest regions in the Vienna area, HCHO and O_3 abundances would have been even higher during JJA19 than occurred.

4. Discussion and conclusions

This study provides a systematic, observation- and model-based analysis of the relationship between HCHO, meteorological parameters, drought indicators, isoprene emissions and ozone for the Vienna region over the period 2018–2020. Particularly, this study addresses the question if HCHO mixing ratios are modulated by BVOC emissions from vegetation. And further, if drought conditions affect plant activity and thus BVOC emissions and if O_3 concentrations are affected by heat and

drought-stressed vegetation. Our results show that HCHO is highly correlated with air temperature, which initiates vegetation metabolism and photosynthetic activity that provides a first indication for a link between observed HCHO and forest BVOC source terms. Furthermore, we find that photosynthetic activity (SIF) correlates with HCHO mixing ratios, but at magnitudes that are dependent on seasonal and meteorological/drought conditions.

To investigate the influence of drought, we contrast separately two spring seasons and two summer seasons, where one spring/summer is characterized by anomalously dry conditions (2020 spring and 2019 summer) and the others serve as reference points (2018 spring and 2020 summer). Our results show that HCHO mixing ratios differ strongly between the dry and reference seasons.

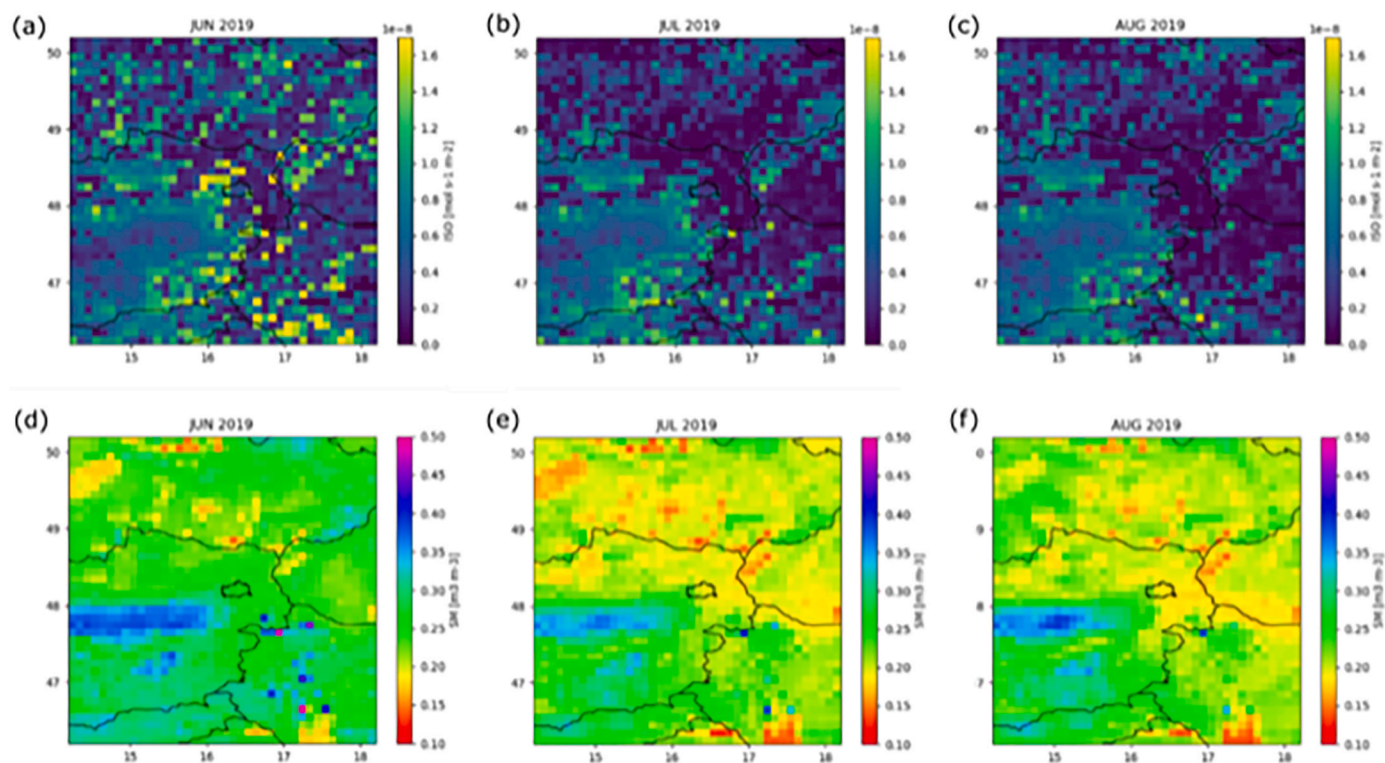During spring 2020, reduced HCHO mixing ratios are found under

Fig. 9. Spatial distribution of isoprene emissions (a)-(c) and the root zone volumetric soil moisture content (d)-(f) during the summer months (from left to right) June, July, and August 2019.
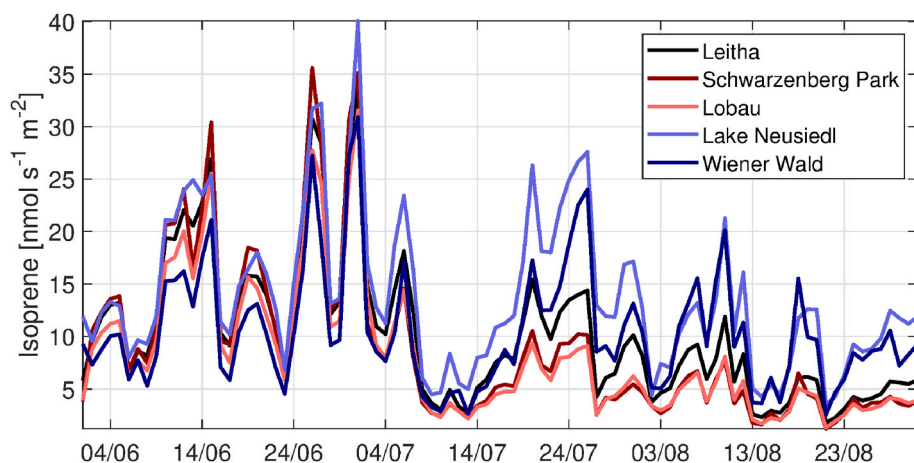

Fig. 10. Time series graph of isoprene emissions (mean over period 08:00–14:00 UTC) simulated with SURFEX-MEGAN3 of different forest areas around the city of Vienna during JJA19 for Leitha (a hilly forest region ~30 km southeast to Vienna), Schwarzenberg Park (a forested area to the immediate west of BOKU within the Vienna city limits), Lobau (a flood plain forest within southeast Vienna ~5 km from city center), LakeNeusiedler (wetland forest ~100 km southeast of Vienna), and Wienerwald (a hilly forest area to the west of Vienna). The units of isoprene emission are nano moles m^{-2} s^{-1}.

the drought conditions (indicated by fAPARa, RSS, VPD, AT, and simulated root zone soil moisture) that led to restricted plant growth at the start of the growing season (reflected in observed and simulated LAI). The reason for these HCHO reductions is reduced plant biomass and photosynthetic activity as a consequence of a pronounced precipitation deficit that leads to reduced BVOC emissions.

Conversely, during summer elevated HCHO mixing ratios are found under the dry 2019 conditions. The SURFEX land surface modelling results indicate that drought affects developed within specific regions around Vienna in July as a result of the hot dry conditions at the end of June, and that some forest regions were impacted by the drought. In June, the hot dry conditions combined with the already established leaves to yield elevated BVOC emissions, despite some reductions in gas-exchange due to drought conditions indicated by higher VPD. Further into July, the drought conditions induce reductions in LAI (observed and

simulated) and photosynthetic activity (represented by SIF) that led to reduced BVOC emissions in the drought affected areas around Vienna. This behaviour of reduced BVOC emissions and the drought-driven mechanisms is reproduced by two BVOC emissions models coupled to the SURFEX land surface model (SURFEX-MEGAN3 in Fig. 10, and SURFEX-MEGAN2.1 in Fig. S5) (Oumami et al., 2022). These results agree with the findings of Zheng et al. (2017), who document for short-term drought with high temperatures a divergence of photosynthetic activity and isoprene emissions. We conclude that despite the reductions in BVOC emissions in some areas, the remaining BVOC emissions, anthropogenic VOC sources, and very active photochemical conditions driven by the hot conditions are enough to maintain high levels of observed HCHO and O_3 during July 2019.

As HCHO can result from primary or secondary sources of both biogenic and anthropogenic origin the individual contributions of these
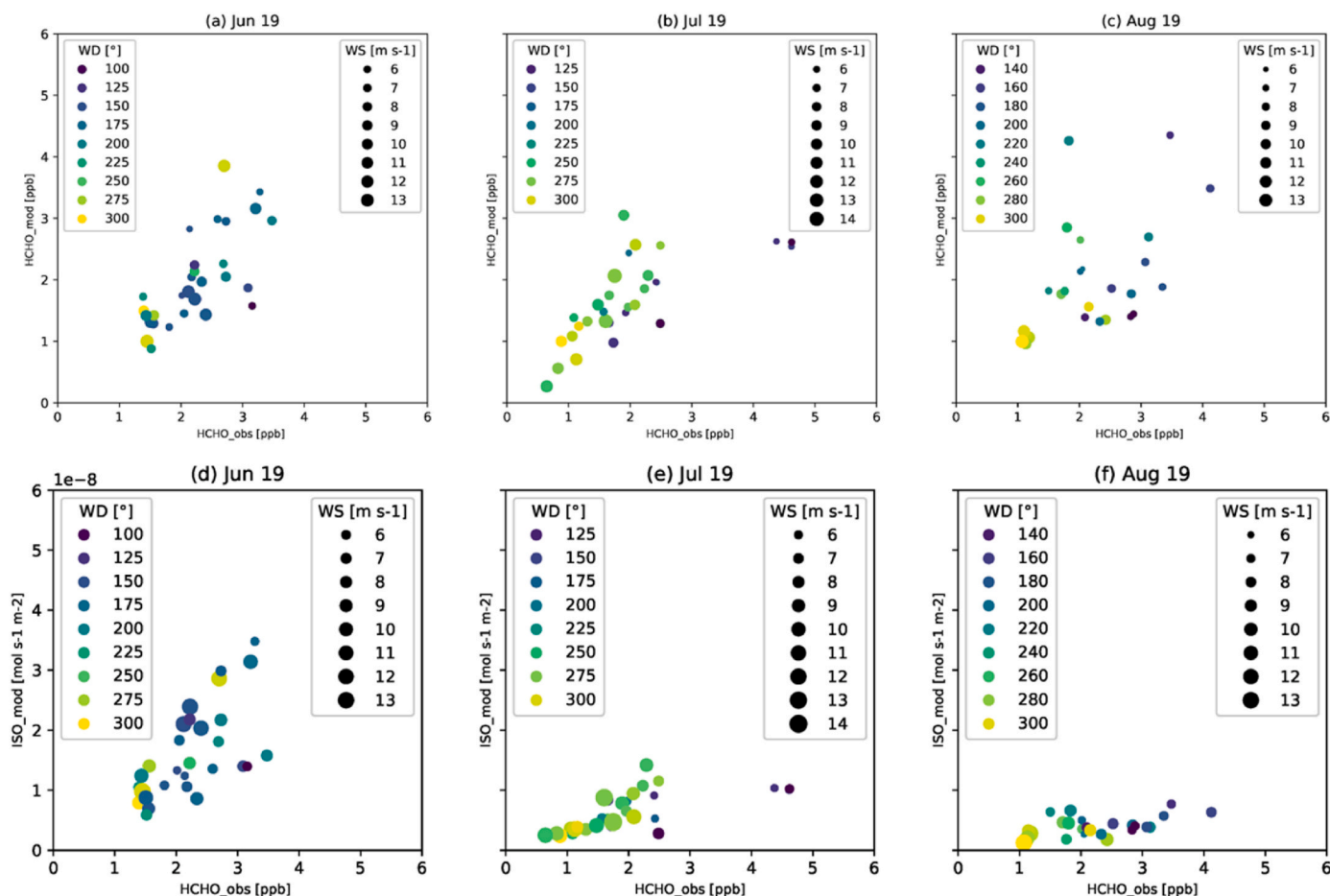
Fig. 11. Scatter plots of HCHO (a)–(c) modelled by MOCAGE and isoprene emissions (d)–(f) modelled by SURFEX-MEGAN3 (both extracted for the Schwarzenberg Park grid box) each compared to observed HCHO. The wind direction (WD) is indicated by color (blue = south easterly; green = southerly; yellow = westerly), wind speed by the sizing of the markers (smallest = 6 m/s, largest = 14 m/s).

to the total HCHO burden have been assessed. Furthermore, for the biogenic fraction the question arises if BVOC emissions are dominated by city trees or nearby forests.

Anthropogenic VOC sources are concentrated in the southeast of the city (refinery, oil port), while the largest forest areas are located in the northwest. Thus, to separate the biogenic and anthropogenic emissions we subsample the available observations based on wind direction (NW, SE). Our analysis shows higher HCHO mixing ratios during flow from the SE compared to the NW. This difference cannot be explained by differences in BVOC emissions as a function of temperature, which indicates a larger anthropogenic contribution to HCHO mixing ratios during SE flow. Therefore, we restricted the further analysis regarding the contribution of BVOC emissions based on wind direction to HCHO mixing ratios and O_3 levels to samples with NW flow. Generally, the dominance of emission from forest areas compared to those from urban trees becomes obvious comparing the total tree density and share of BVOC emitter species. The tree density of forest is up to two magnitudes higher than within the city. While roughly 50% of the trees in the forests surrounding Vienna are strong BVOC emitters (standard emission potential of above 20 $\mu g\ gdw^{-1}\ h^{-1}$), this is only true for about 8% of urban trees. These results are fully reflected in the maps of SURFEX-MEGAN3 isoprene emissions from the region around Vienna.

We analysed further how O_3 concentrations are affected by heat and drought-stressed vegetation. Our results show that drought conditions lead to lowered O_3 amounts during spring (driven strongly by reduced BVOC emission), and elevated O_3 amounts during summer (driven by warm temperatures and potentially reduced deposition). The O_3 reduction during the spring of 2020 is of particular interest given that

reduced O_3 levels occurred despite 17% higher global radiation, which illustrates the strong potential of BVOC emissions to modulate urban O_3 burdens. Conversely, our results for summer illustrate an importance of drought conditions for elevated O_3 levels, which agrees with the findings from Lin et al. (2020) for an Italian oak forest and a Dutch spur forest for the droughts in August 2003 and June 1992. The evidence provided by the MOCAGE simulations of HCHO based on the SURFEX-MEGAN isoprene emissions in summer 2019 suggest that while the drought caused large reductions in BVOC emissions some specific forest regions remained as strong BVOC emitters and that the hot conditions accompanying the drought led to strong emissions. This suggests that in cases where droughts do not fully suppress BVOC emissions from forests, the associated hot conditions can lead to elevated O_3.

As the analysis is only based on a single season to single season comparison, and drought conditions can develop in a spatially diverse manner, it is still not possible to draw general conclusions. Drought can affect regional transport patterns by prolonging high pressure systems, thus slowing down wind speed and stimulating the south-easterly flow that is associated to such conditions in Vienna. The interrelation between drought, BVOC, HCHO, and O_3 should be investigated further at this site with longer time series.

Further reductions of NO_x emissions could have an impact on urban O_3 levels. To discuss this, it can be noted that the first CoV-2 lockdown (March 16, 2020–April 14, 2020) of Austria coincided with the selected dry spring period studied here. Given that O_3 production in urban areas in Austria are generally VOC limited (Karl et al., 2017; Mayer et al., 2022), a reduction of NOx is of minor significance in Vienna. Lamprecht et al. (2021) for example observed a decrease of ozone during Austria's

CoV-2 lockdown due to decreasing NO emissions but showed that O_x remained constant. Similarly, Staehle et al. (2022) highlight elevated nighttime titration.

Future changes in CO_2 levels will matter, not only due to their effect on climate warming. On the one hand CO_2 fertilization may lead to increased plant growth and subsequently more abundant biomass and higher LAIs (Zhu et al., 2016), which could regionally lead to higher BVOC emissions and thus O_3 burdens. On the other hand, higher CO_2 levels can suppress BVOC emission, which is known as CO_2 inhibition (Possell and Hewitt, 2011; Wilkinson et al., 2009) and could limit BVOC supply for urban O_3 production. Investigating such effects of changes in future atmospheric composition, climate and vegetation is beyond the scope of the present study and suggested for future modelling work.

CRediT authorship contribution statement

Heidelinde Trimmel: Conceptualization, Methodology, Software, Formal analysis, Investigation, Writing – original draft, Writing – review & editing, Visualization, Project administration, Funding acquisition. **Paul Hamer:** Writing – review & editing, scientific analysis, and SURFEX-MEGAN3 modelling. **Monika Mayer:** Methodology, Resources, Writing – original draft. **Stefan F. Schreier:** Resources, Writing – review & editing. **Philipp Weihs:** Writing – review & editing. **Josef Eitzinger:** Resources, Writing – review & editing. **Hans Sandén:** Funding acquisition, Project administration. **Anne Charlott Fitzky:** Writing – review & editing. **Andreas Richter:** Resources, Writing – review & editing. **Jean-Christophe Calvet:** Software, design of study and simulations using the SURFEX land surface model. **Bertrand Bonan:** Software, design of study and simulations using the SURFEX land surface model. **Catherine Meurey:** Software, design of study and simulations using the SURFEX land surface model. **Islen Vallejo:** Software, programming and development of the SURFEX-MEGAN3 BVOC model coupling. **Sabine Eckhardt:** Software, Visualization, data acquisition and programming for SURFEX-MEGAN3 BVOC model coupling. **Gabriela Sousa Santos:** Software, programming and development of the SURFEX-MEGAN3 BVOC model coupling. **Safae Oumami:** Software, Investigation, Coupling of SURFEX-MEGAN2.1 and modelling. **Joaquim Arteta:** Software, Coupling of SURFEX-MEGAN2.1. **Virginie Marécal:** Writing – review & editing. **Leonor Tarrasón:** Project administration, and design of scientific modelling studies. **Thomas Karl:** Writing – review & editing. **Harald E. Rieder:** Resources, Writing – review & editing.

Declaration of competing interest

The authors declare that they have no known competing financial interests or personal relationships that could have appeared to influence the work reported in this paper.

Data availability

Data will be made available on request.

Appendix A. Supplementary data

Supplementary data to this article can be found online at https://doi.org/10.1016/j.atmosenv.2023.119768.

References

Agro Drought Austria, 2021. https://ada.boku.ac.at/. last access: 17.4.2023.

Albergel, C., Dutra, E., Bonan, B., Zheng, Y., Munier, S., Balsamo, G., de Rosnay, P., Muñoz-Sabater, J., Calvet, J.-C., 2019. Monitoring and forecasting the impact of the 2018 summer heatwave on vegetation. Remote Sens. 11 (5), 520. https://doi.org/10.3390/rs11050520.

Albergel, C., Munier, S., Leroux, D.J., Dewaele, H., Fairbairn, D., Barbu, A.L., Gelati, E., Dorigo, W., Faroux, S., Meurey, C., Le Moigne, P., Decharme, B., Mahfouf, J.-F, Calvet, J.-C., 2017. Sequential assimilation of satellite-derived vegetation and soil moisture products using SURFEX_v8.0: LDAS-Monde assessment over the Euro-Mediterranean area. Geosci. Model Dev. 10, 3889–3912. https://doi.org/10.5194/gmd-10-3889-2017.

Arlander, D.W., Brüning, D., Schmidt, U., Ehhalt, D.H., 1995. The tropospheric distribution of formaldehyde during TROPOZ II. J. Atmos. Chem. 22 (3), 251–269. https://doi.org/10.1007/BF00696637.

Bacour, C., Maignan, F., MacBean, N., Porcar-Castell, A., Flexas, J., Frankenberg, C., Peylin, P., Chevallier, F., Vuichard, N., Bastrikov, V., 2019a. Improving estimates of gross primary productivity by assimilating solar-induced fluorescence satellite retrievals in a terrestrial biosphere model using a process-based SIF model. J. Geophys. Res.: Biogeosciences 124 (11), 3281–3306. https://doi.org/10.1029/2019JG005040.

Bacour, C., Maignan, F., Peylin, P., MacBean, N., Bastrikov, V., Joiner, J., Köhler, P., Guanter, L., Frankenberg, C., 2019b. Differences between OCO-2 and GOME-2 SIF products from a model-data fusion perspective. J. Geophys. Res. Biogeosci. 124, 3143–3157. https://doi.org/10.1029/2018JG004938.

Baghi, R., Helmig, D., Guenther, A., Duhl, T., Daly, R., 2012. Contribution of flowering trees to urban atmospheric biogenic volatile organic compound emissions. Biogeosciences 9 (10), 3777–3785. https://doi.org/10.5194/bg-9-3777-2012.

Bauwens, M., Stavrakou, T., Müller, J.-F., De Smedt, I., Van Roozendael, M., van der Werf, G.R., Wiedinmyer, C., Kaiser, J.W., Sindelarova, K., Guenther, A., 2016. Nine years of global hydrocarbon emissions based on source inversion of OMI formaldehyde observations. Atmos. Chem. Phys. 16 (15), 10133–10158. https://doi.org/10.5194/acp-16-10133-2016.

Bauwens, M., Stavrakou, T., Müller, J.-F., Schaeybroeck, B.V., Cruz, L.D., Troch, R.D., Giot, O., Hamdi, R., Termonia, P., Laffineur, Q., Amelynck, C., Schoon, N., Heinesch, B., Holst, T., Arneth, A., Ceulemans, R., Sanchez-Lorenzo, A., Guenther, A., 2018. Recent Past (1979–2014) and Future (2070–2099) Isoprene FLuxes over Europe Simulated with the MEGAN–MOHYCAN Model, vol. 18.

Bousserez, N., Attié, J.L., Peuch, V.H., Michou, M., Pfister, G., Edwards, D., Emmons, L., Mari, C., Barret, B., Arnold, S.R., Heckel, A., Richter, A., Schlager, H., Lewis, A., Avery, M., Sachse, G., Browell, E.V., Hair, J.W., 2007. Evaluation of the MOCAGE chemistry transport model during the ICARTT/ITOP experiment. J. Geophys. Res. Atmos. 112, D10. https://doi.org/10.1029/2006JD007595.

Bonn, B., Magh, R.-K., Rombach, J., Kreuzwieser, J., 2019. Biogenic isoprenoid emissions under drought stress: different responses for isoprene and terpenes. Biogeosciences 16 (23), 4627–4645. https://doi.org/10.5194/bg-16-4627-2019.

Bréda, N.J., 2003. Ground-based measurements of leaf area index: a review of methods, instruments and current controversies. J. Exp. Bot. 54 (392), 2403–2417.

Bundesforschungszentrum für Wald, 2021. Waldinventur 2007-2009. https://bfw.ac.at/ (last access: 11 June 2022).

Calfapietra, C., Fares, S., Manes, F., Morani, A., Sgrigna, G., Loreto, F., 2013. Role of Biogenic Volatile Organic Compounds (BVOC) emitted by urban trees on ozone concentration in cities: a review. Environ. Pollut. 183, 71–80. https://doi.org/10.1016/j.envpol.2013.03.012.

Calvet, J.-C., Noilhan, J., 2000. From near-surface to root-zone soil moisture using year-round data. J. Hydrometeorol. 1 (5), 393–411. https://doi.org/10.1175/1525-7541(2000)001<0393:FNSTRZ>2.0.CO;2.

Calvet, J.-C., Noilhan, J., Roujean, J.-L., Bessemoulin, P., Cabelguenne, M., Olioso, A., Wigneron, J.-P., 1998. An interactive vegetation SVAT model tested against data from six contrasting sites. Agric. For. Meteorol. 92 (2), 73–95. https://doi.org/10.1016/S0168-1923(98)00091-4.

Calvet, J.-C., Rivalland, V., Picon-Cochard, C., Guehl, J.-M., 2004. Modelling forest transpiration and CO2 fluxes—response to soil moisture stress. Agric. For. Meteorol. 124 (3–4), 143–156. https://doi.org/10.1016/j.agrformet.2004.01.007.

Checa-Garcia, R., Hegglin, M.I., Kinnison, D., Plummer, D.A., Shine, K.P., 2018. Historical tropospheric and stratospheric ozone radiative forcing using the CMIP6 database. Geophys. Res. Lett. 45 (7), 3264–3273. https://doi.org/10.1002/2017GL076770.

Cho, K., Tiwari, S., Agrawal, S.B., Torres, N.L., Agrawal, M., Sarkar, A., Shibato, J., Agrawal, G.K., Kubo, A., Rakwal, R., 2011. Tropospheric ozone and plants: absorption, responses, and consequences. In: Whitacre, D.M. (Ed.), Reviews of Environmental Contamination and Toxicology Volume 212, Reviews of Environmental Contamination and Toxicology. Springer New York, New York, NY, pp. 61–111. https://doi.org/10.1007/978-1-4419-8453-1_3.

City of Vienna, 2021. Baumkataster. https://www.wien.gv.at/umweltgut/public/grafik.aspx?ThemePage=11. last access: 17 April 2023.

Clifton, O.E., Paulot, F., Fiore, A.M., Horowitz, L.W., Correa, G., Baublitz, C.B., Fares, S., Goded, I., Goldstein, A.H., Gruening, C., Hogg, A.J., Loubet, B., Mammarella, I., Munger, J.W., Neil, L., Stella, P., Uddling, J., Vesawenig, T., Weng, E., 2020. Influence of dynamic ozone dry deposition on ozone pollution. J. Geophys. Res. 21

Copernicus, 2021. https://land.copernicus.eu/pan-european/corine-land-cover. last access: 17 April 2023.

Crowther, T.W., Glick, H.B., Covey, K.R., Bettigole, C., Maynard, D.S., Thomas, S.M., Smith, J.R., Hintler, G., Duguid, M.C., Amatulli, G., Tuanmu, M.-N., Jetz, W., Salas, C., Stam, C., Piotto, D., Tavani, R., Green, S., Bruce, G., Williams, S.J., Wiser, S.K., Huber, M.O., Hengeveld, G.M., Nabuurs, G.-J., Tikhonova, E., Borchardt, P., Li, C.-F., Powrie, L.W., Fischer, M., Hemp, A., Homeier, J., Cho, P., Vibrans, A.C., Umunay, P.M., Piao, S.L., Rowe, C.W., Ashton, M.S., Crane, P.R., Bradford, M.A., 2015. Mapping tree density at a global scale. Nature 525, 201–205. https://doi.org/10.1038/nature14967.

Curci, G., Palmer, P.I., Kurosu, T.P., Chance, K., Visconti, G., 2010. Estimating European volatile organic compound emissions using satellite observations of formaldehyde from the Ozone Monitoring Instrument. Atmos. Chem. Phys. 10, 11501–11517. https://doi.org/10.5194/acp-10-11501-2010.

De Smedt, I., Stavrakou, T., Müller, J.-F., van der A, R.J., Van Roozendael, M., 2010. Trend detection in satellite observations of formaldehyde tropospheric columns. Geophys. Res. Lett. 37 https://doi.org/10.1029/2010GL044245 n/a-n/a.

Demetillo, M.A.G., Anderson, J.F., Geddes, J.A., Yang, X., Najacht, E.Y., Herrera, S.A., Kabasares, K.M., Kotsakis, A.E., Lerdau, M.T., Pusede, S.E., 2019. Observing severe drought influences on ozone air pollution in California. Environ. Sci. Technol. 53, 4695–4706. https://doi.org/10.1021/acs.est.8b04852.

Dingman, S.L., 2002. Physical Hydrology, second ed. Prentice Hall, New Jersey.

Dufour, A., Amodei, M., Ancellet, G., Peuch, V.H., 2005. Observed and modelled "chemical weather" during ESCOMPTE. Atmos. Res. 74 (1–4), 161–189.

Environment Agency Austria, Anderl, M., Haider, S., Lampert, C., Perl, D., Pinterits, M., Poupa, S., Purzner, M., Schieder, W., Schmidt, G., Schodl, B., Titz, M., Wieser, M., 2021. Austria's Annual Air Emission Inventor– 1990-2019 - Emissions of SO2, NOx, NMVOC, NH3, PM2.5 (No. REP-0760). With assistance of. Umweltbundesamt GmbH, Vienna, Austria.

European Drought Observatory, 2021a. EDO Standardized Precipitation Index, 3-month Accumulation Period (SPI-3), Blended and Interpolated (Version 1.2.0). European Commission, Joint Research Centre (JRC) PID: https://data.jrc.ec.europa.eu/dataset/0ae4cbf0-55f1-4aee-b1ae-a5317b264072. last access: 11.6.2022.

European Drought Observatory, 2021b. EDO Fraction of Absorbed Photosynthetically Active Radiation (FAPAR) Anomaly (MODIS) (Version 1.3.1). European Commission, Joint Research Centre (JRC) PID. http://data.europa.eu/89h/91a222a0-74fe-468f-b53a-b622aa1161cf. last access: 11.6.2022.

European Environment Agency, 2020. Air Quality in Europe: 2020 Report. Publications Office, LU.

European Environment Agency, 2021. DiscoMap. https://discomap.eea.europa.eu/map/fme/AirQualityExport.htm. last access: 17 April 2023.

El Amraoui, L., Semane, N., Peuch, V.H., Santee, M.L., 2008. Investigation of dynamical processes in the polar stratospheric vortex during the unusually cold winter 2004/2005. Geophys. Res. Lett. 35 (3).

Emberson, L.D., Büker, P., Ashmore, M.R., 2007. Assessing the risk caused by ground level ozone to European forest trees: a case study in pine, beech and oak across different climate regions. Environ. Pollut. 147 (3), 454–466. https://doi.org/10.1016/j.envpol.2006.10.026.

Fairbairn, D., Barbu, A.L., Napoly, A., Albergel, C., Mahfouf, J.-F., Calvet, J.-C., 2017. The effect of satellite-derived surface soil moisture and leaf area index land data assimilation on streamflow simulations over France. Hydrol. Earth Syst. Sci. 21, 2015–2033. https://doi.org/10.5194/hess-21-2015-2017.

Fares, S., Oksanen, E., Lännenpää, M., Julkunen-Tiitto, R., Loreto, F., 2010. Volatile emissions and phenolic compound concentrations along a vertical profile of Populus nigra leaves exposed to realistic ozone concentrations. Photosynth. Res. 104, 61–74. https://doi.org/10.1007/s11120-010-9549-5.

Faroux, S., Kaptué Tchuenté, A.T., Roujean, J.-L., Masson, V., Martin, E., Le Moigne, P., 2013. ECOCLIMAP-II/Europe: a twofold database of ecosystems and surface parameters at 1 km resolution based on satellite information for use in land surface, meteorological and climate models. Geosci. Model Dev. (GMD) 6, 563–582. https://doi.org/10.5194/gmd-6-563-2013.

Ferracci, V., Bolas, C.G., Freshwater, R.A., Staniaszek, Z., King, T., Iars, K., Otu-Larbi, F., Beale, J., Malhi, Y., Waine, T.W., Jones, R.L., Ashworth, K., Harris, N.R.P., 2020. Continuous isoprene measurements in a UK temperate forest for a whole growing season: effects of drought stress during the 2018 heatwave. Geophys. Res. Lett. 11.

Fitzky, A.C., Kaser, L., Peron, A., Karl, T., Graus, M., Tholen, D., Halbwirth, H., Trimmel, H., Pesendorfer, M., Rewald, B., Sandén, H., 2023. Same, same, but different: Drought and salinity affect BVOC emission rate and alter blend composition of urban trees. Urban For. Urban Green. 80 https://doi.org/10.1016/j.ufug.2023.127842.

Fu, T.-M., Jacob, D.J., Palmer, P.I., Chance, K., Wang, Y.X., Barletta, B., Blake, D.R., Stanton, J.C., Pilling, M.J., 2007. Space-based formaldehyde measurements as constraints on volatile organic compound emissions in east and south Asia and implications for ozone. J. Geophys. Res. 112, D06312 https://doi.org/10.1029/2006JD007853.

Fu, P., Meacham-Hensold, K., Siebers, M.H., Bernacchi, C.J., 2021. The inverse relationship between solar-induced fluorescence yield and photosynthetic capacity: benefits for field phenotyping. J. Exp. Bot. 72 (4), 1295–1306. https://doi.org/10.1093/jxb/eraa537.

Fuster, B., Sánchez-Zapero, J., Camacho, F., García-Santos, V., Verger, A., Lacaze, R., Weiss, M., Baret, F., Smets, B., 2020. Quality assessment of PROBA-V LAI, fAPAR and fCOVER collection 300 m products of Copernicus global land service. Rem. Sens. 12, 1017. https://doi.org/10.3390/rs12061017.

Guanter, L., Aben, I., Tol, P., Krijger, J.M., Hollstein, A., Köhler, P., Damm, A., Joiner, J., Frankenberg, C., Landgraf, J., 2015. Potential of the TROPOspheric Monitoring Instrument (TROPOMI) onboard the Sentinel-5 Precursor for the monitoring of terrestrial chlorophyll fluorescence. Atmos. Meas. Tech. 8, 1337–1352. https://doi.org/10.5194/amt-8-1337-2015.

Guenther, A.B., Jiang, X., Heald, C.L., Sakulyanontvittaya, T., Duhl, T., Emmons, L.K., Wang, X., 2012. The Model of Emissions of Gases and Aerosols from Nature version 2.1 (MEGAN2.1): an extended and updated framework for modeling biogenic emissions. Geosci. Model Dev. (GMD) 5 (6), 1471–1492. https://doi.org/10.5194/gmd-5-1471-2012.

Guenther, A., Jiang, X., Shah, T., Huang, L., Kemball-Cook, S., Yarwood, G., 2020. Model of emissions of gases and aerosol from nature version 3 (MEGAN3) for estimating biogenic emissions. In: Mensink, C., Gong, W., Hakami, A., Hrsg (Eds.), Air Pollution Modeling and its Application XXVI (S. 187–192). Springer International Publishing. https://doi.org/10.1007/978-3-030-22055-6_29.

Guth, J., Josse, B., Marécal, V., Joly, M., Hamer, P., 2016. First implementationof secondary inorganic aerosols in the MOCAGEversion R2.15.0 chemistry transport model. Geosci. Model Dev. 9, 137–160. https://doi.org/10.5194/gmd-9-137-2016.

Haiden, T., Kann, A., Wittmann, C., Pistotnik, G., Bica, B., Gruber, C., 2011. The integrated nowcasting through comprehensive analysis (INCA) system and its validation over the eastern alpine region. Weather Forecast. 26, 166–183. https://doi.org/10.1175/2010WAF2222451.1.

Honoré, C., Rouïl, L., Vautard, R., Beekmann, M., Bessagnet, B., Dufour, A., Elichegaray, C., Flaud, J-M., Malherbe, L., Meleux, F., 2008. Predictability of European air quality: assessment of 3 years of operational forecasts and analyses by the PREV'AIR system. J. Geophys. Res. Atmos. 113, D04301 https://doi.org/10.1029/2007JD008761.

IPCC, 2021: *Climate Change 2021: The Physical Science Basis. Contribution of Working Group I to the Sixth Assessment Report of the Intergovernmental Panel on Climate Change* [Masson-Delmotte, V., P. Zhai, A. Pirani, S.L. Connors, C. Péan, S. Berger, N. Caud, Y. Chen, L. Goldfarb, M.I. Gomis, M. Huang, K. Leitzell, E. Lonnoy, J.B.R. Matthews, T. K. Maycock, T. Waterfield, O. Yelekçi, R. Yu, and B. Zhou (eds.)]. Cambridge University Press, Cambridge, United Kingdom and New York, NY, USA, In press, doi: 10.1017/9781009157896.

Jia, G., Shevliakova, E., Artaxo, P., De Noblet-Ducoudré, N., Houghton, R., House, J., Kitajima, K., Lennard, C., Popp, A., Sirin, A., Sukumar, R., Verchot, L., 2019. Land–climate interactions. In: Shukla, P.R., Skea, J., Calvo Buendia, E., Masson-Delmotte, V., Pörtner, H.-O., Roberts, D., Zhai, P., Slade, R., Connors, S., van Diemen, R., Ferrat, M., Haughey, E., Luz, S., Neogi, S., Pathak, M., Petzold, J., Portugal Pereira, J., Vyas, P., Huntley, E., Malley, J. (Eds.), Climate Change and Land: an IPCC Special Report on Climate Change, Desertification, Land Degradation, Sustainable Land Management, Food Security, and Greenhouse Gas Fluxes in Terrestrial Ecosystems.

Karl, M., Guenther, A., Koble, R., Leip, A., Seufert, G., 2009. A New European Plant-Specific Emission Inventory of Biogenic Volatile Organic Compounds for Use in Atmospheric Transport Models 29.

Josse, B., Simon, P., Peuch, V.H., 2004. Radon global simulations with the multiscale chemistry and transport model MOCAGE. Tellus B 56 (4), 339–356.

Karl, T., Graus, M., Striednig, M., Lamprecht, C., Hammerle, A., Wohlfahrt, G., Held, A., von der Heyden, L., Deventer, M.J., Krismer, A., Haun, C., Feichter, R., Lee, J., 2017. Urban eddy covariance measurements reveal significant missing NOx emissions in Central Europe. Sci. Rep. 7 (1), 2536. https://doi.org/10.1038/s41598-017-02699-9.

Kleist, E., Mentel, T.F., Andres, S., Bohne, A., Folkers, A., Kiendler-Scharr, A., Rudich, Y., Springer, M., Tillmann, R., Wildt, J., 2012. Irreversible impacts of heat on the

emissions of monoterpenes, sesquiterpenes, phenolic BVOC and green leaf volatiles from several tree species. Biogeosciences 9 (12), 5111–5123. https://doi.org/10.5194/bg-9-5111-2012.

Köhler, P., Frankenberg, C., Magney, T.S., Guanter, L., Joiner, J., Landgraf, J., 2018. Global retrievals of solar-induced chlorophyll fluorescence with TROPOMI: first results and intersensor comparison to OCO-2. Geophys. Res. Lett. 45 (10), 456. https://doi.org/10.1029/2018GL079031, 10,463.

Kurucz, R.L., Furenhild, I., Brault, J., Testermann, L., 1984. Solar Flux Atlas from 296 to 1300 Nm, National Solar Observatory Atlas No. 1. June.

Lamotte, C., Guth, J., Marécal, V., Cussac, M., Hamer, P.D., Theys, N., Schneider, P., 2021. Modeling study of the impact of SO_2 volcanic passive emissions on the tropospheric sulfur budget. Atmos. Chem. Phys. 21, 11379–11404. https://doi.org/10.5194/acp-21-11379-2021.

Lamprecht, C., Graus, M., Striednig, M., Stichaner, M., Karl, T., 2021. Decoupling of urban CO_2 and air pollutant emission reductions during the European SARS-CoV-2 lockdown. Atmos. Chem. Phys. 21 (4), 3091–3102. https://doi.org/10.5194/acp-21-3091-2021.

Larcher, W., 2003. Physiological Plant Ecology: Ecophysiology and Stress Physiology of Functional Groups, fourth ed. Springer, Berlin; New York.

Lefevre, F., Brasseur, G.P., Folkins, I., Smith, A.K., Simon, P., 1994. Chemistry of the 1991–1992 stratospheric winter: three-dimensional model simulations. J. Geophys. Res. Atmos. 99, 8183–8195.

Lin, M., Horowitz, L.W., Xie, Y., Paulot, F., Malyshev, S., Shevliakova, E., Finco, A., Gerosa, G., Kubistin, D., Pilegaard, K., 2020. Vegetation feedbacks during drought exacerbate ozone air pollution extremes in Europe. Nat. Clim. Change 10, 444–451. https://doi.org/10.1038/s41558-020-0743-y.

Louis, J.F., 1979. A parametric model of vertical eddy fluxes in the atmosphere. Boundary-Layer Meteorol. 17 (2), 187–202.

MacDonald, S.M., Oetjen, H., Mahajan, A.S., Whalley, L.K., Edwards, P.M., Heard, D.E., Jones, C.E., Plane, J.M.C., 2012. DOAS measurements of formaldehyde and glyoxal above a south-east Asian tropical rainforest. Atmos. Chem. Phys. 12 (13), 5949–5962. https://doi.org/10.5194/acp-12-5949-2012.

Marais, E.A., Jacob, D.J., Guenther, A., Chance, K., Kurosu, T.P., Murphy, J.G., Reeves, C.E., Pye, H.O.T., 2014. Improved model of isoprene emissions in Africa using Ozone Monitoring Instrument (OMI) satellite observations of formaldehyde: implications for oxidants and particulate matter. Atmos. Chem. Phys. 14 (15), 7693–7703. https://doi.org/10.5194/acp-14-7693-2014.

Masson, V., Champeaux, J.-L., Chauvin, F., Meriguet, C., Lacaze, R., 2003. A global database of land surface parameters at 1-km resolution in meteorological and climate models. J. Clim. 16 (9), 1261–1282.

Masson, V., Le Moigne, P., Martin, E., Faroux, S., Alias, A., Alkama, R., Belamari, S., Barbu, A., Boone, A., Bouyssel, F., Brousseau, P., Brun, E., Calvet, J.-C., Carrer, D., Decharme, B., Delire, C., Donier, S., Essaouini, K., Gibelin, A.-L., Giordani, H., Habets, F., Jidane, M., Kerdraon, G., Kourzeneva, E., Lafaysse, M., Lafont, S., Lebeaupin Brossier, C., Lemonsu, A., Mahfouf, J.-F., Marguinaud, P., Mokhtari, M., Morin, S., Pigeon, G., Salgado, R., Seity, Y., Taillefer, F., Tanguy, G., Tulet, P., Vincendon, B., Vionnet, V., Voldoire, A., 2013. The SURFEXv7.2 land and ocean surface platform for coupled or offline simulation of earth surface variables and fluxes. Geosci. Model Dev. 6, 929–960. https://doi.org/10.5194/gmd-6-929-2013.

Mayer, M., Schreier, S.F., Spangl, W., Staehle, C., Trimmel, H., Rieder, H.E., 2022. An analysis of 30 years of surface ozone concentrations in Austria: temporal evolution, changes in precursor emissions and chemical regimes, temperature dependence, and lessons for the future. Environ. Sci. J. Integr. Environ. Res.: Atmosphere. https://doi.org/10.1039/D2EA00004K.

Meroni, M., Rossini, M., Guanter, L., Alonso, L., Rascher, U., Colombo, R., Moreno, J., 2009. Remote sensing of solar-induced chlorophyll fluorescence: review of methods and applications. Rem. Sens. Environ. 113 (10), 2037–2051. https://doi.org/10.1016/j.rse.2009.05.003.

Millet, D.B., Jacob, D.J., Boersma, K.F., Fu, T.-M., Kurosu, T.P., Chance, K., Heald, C.L., Guenther, A., 2008. Spatial distribution of isoprene emissions from North America derived from formaldehyde column measurements by the OMI satellite sensor. J. Geophys. Res. 113 (D2), D02307 https://doi.org/10.1029/2007JD008950.

Niinemets, Ü., 2010. Mild versus severe stress and BVOCs: thresholds, priming and consequences. Trends Plant Sci. 15 (3), 145–153. https://doi.org/10.1016/j.tplants.2009.11.008.

Nowak, D.J., Crane, D.E., Stevens, J.C., Ibarra, M., 2002. Brooklyn's Urban Forest (NE-GTR-290; P. NE-GTR-290). U.S. Department of Agriculture, Forest Service, Northeastern Research Station. https://doi.org/10.2737/NE-GTR-290.

Oderbolz, D.C., Aksoyoglu, S., Keller, J., Barmpadimos, I., Steinbrecher, R., Skjøth, C.A., Plaß-Dülmer, C., Prévôt, A.S.H., 2013. A comprehensive emission inventory of biogenic volatile organic compounds in Europe: improved seasonality and land-cover. Atmos. Chem. Phys. 13, 1689–1712. https://doi.org/10.5194/acp-13-1689-2013.

Oumami, S., Arteta, J., Guidard, V., 2022. Evaluation of Biogenic Emissions from SURFEX-MEGAN2, vol. 1 (In preparation).

Palmer, P.I., Jacob, D.J., Fiore, A.M., Martin, R.V., Chance, K., Kurosu, T.P., 2003. Mapping isoprene emissions over North America using formaldehyde column observations from space. J. Geophys. Res. Atmos. 108 https://doi.org/10.1029/2002JD002153, 2002JD002153.

Parrish, D.D., Ryerson, T.B., Mellqvist, J., Johansson, J., Fried, A., Richter, D., Walega, J.G., Washenfelder, R.A., de Gouw, J.A., Peischl, J., Aikin, K.C., McKeen, S.A., Frost, G.J., Fehsenfeld, F.C., Herndon, S.C., 2012. Primary and secondary sources of formaldehyde in urban atmospheres: Houston Texas region. Atmos. Chem. Phys. 12, 3273–3288. https://doi.org/10.5194/acp-12-3273-2012.

Peñuelas, J., Staudt, M., 2010. BVOCs and global change. Trends Plant Sci. 15 (3), 133–144. https://doi.org/10.1016/j.tplants.2009.12.005.

Peron, A., Kaser, L., Fitzky, A.C., Graus, M., Halbwirth, H., Greiner, J., Wohlfahrt, G., Rewald, B., Sandén, H., Karl, T., 2021. Combined effects of ozone and drought stress on the emission of biogenic volatile organic compounds from *Quercus robur* L. Biogeosciences 18 (2), 535–556. https://doi.org/10.5194/bg-18-535-2021.

Schoetter, R., Kwok, Y.T., de Munck, C., Lau, K.K.L., Wong, W.K., Masson, V., 2020. Multi-layer coupling between SURFEX-TEB-v9.0 and Meso-NH-v5.3 for modelling the urban climate of high-rise cities. Geosci. Model Dev. 13 (11), 5609–5643. https://doi.org/10.5194/gmd-13-5609-2020.

Possell, M., Hewitt, C.N., 2011. Isoprene emissions from plants are mediated by atmospheric CO_2 concentrations. Global Change Biology 17 (4), 1595–1610.

Scholz, L., 2019. Estimation of the Potential BVOC Emissions by the Different Tree Species in Malmö.

Schreier, S.F., Richter, A., Peters, E., Ostendorf, M., Schmalwieser, A.W., Weihs, P., Burrows, J.P., 2020. Dual ground-based MAX-DOAS observations in Vienna, Austria: evaluation of horizontal and temporal NO2, HCHO, and CHOCHO distributions and comparison with independent data sets. Atmos. Environ. X 5, 100059. https://doi.org/10.1016/j.aeaoa.2019.100059.

Seco, R., Karl, T., Guenther, A., Hosman, K.P., Pallardy, S.G., Gu, L., Geron, C., Harley, P., Kim, S., 2015. Ecosystem-scale volatile organic compound fluxes during an extreme drought in a broadleaf temperate forest of the Missouri Ozarks (central USA). Global Change Biol. 21 (10), 3657–3674. https://doi.org/10.1111/gcb.12980.

Simpson, D., Winiwarter, W., Börjesson, G., Cinderby, S., Ferreiro, A., Guenther, A., Hewitt, C.N., Janson, R., Khalil, M.A.K., Owen, S., Pierce, T.E., Puxbaum, H., Shearer, M., Skiba, U., Steinbrecher, R., Tarrasón, L., Öquist, M.G., 1999. Inventorying emissions from nature in Europe. J. Geophys. Res. Atmos. 104, 8113–8152. https://doi.org/10.1029/98JD02747.

Sterckx, S., Benhadj, I., Duhoux, G., Livens, S., Dierckx, W., Goor, E., Adriaensen, S., Heyns, W., Van Hoof, V., Strackx, G., Nackaerts, K., Reusen, I., Van Achteren, T., Dries, J., Van Roey, T., Mellab, K., Duca, R., Zender, J., 2014. The PROBA-V mission: image processing and calibration. Int. J. Rem. Sens. 35 (7), 2565–2588. https://doi.org/10.1080/01431161.2014.883094.

Staehle, C., Mayer, M., Kirchsteiger, B., Klaus, V., Kult-Herdin, J., Schmidt, C., Schreier, S., Karlicky, J., Trimmel, H., Kasper-Giebl, A., Scherllin-Pirscher, B., Rieder, H., 2022. Quantifying changes in ambient NO_x, O_3 and PM10 concentrations in Austria during the COVID-19 related lockdown in spring 2020. Air Qual. Atmos. Health. 15, 1993–2007. https://doi.org/10.1007/s11869-022-01232-w.

Stockwell, W.R., Kirchner, F., Kuhn, M., Seefeld, S., 1997. A new mechanism for regional atmospheric chemistry modeling. J. Geophys. Res. Atmos. 102 (D22), 25847–25879.

Stoy, P.C., Trowbridge, A.M., Siqueira, M.B., Freire, L.S., Phillips, R.P., Jacobs, L., Wiesner, S., Monson, R.K., Novick, K.A., 2021. Vapor pressure deficit helps explain biogenic volatile organic compound fluxes from the forest floor and canopy of a temperate deciduous forest. Oecologia 197, 971–988. https://doi.org/10.1007/s00442-021-04891-1.

Teng, H., Branstator, G., Tawfik, A.B., Callaghan, P., 2019. Circumglobal response to prescribed soil moisture over north America. J. Clim. 32 (14), 4525–4545. https://doi.org/10.1175/JCLI-D-18-0823.1.

Teskey, R., Wertin, T., Bauweraerts, I., Ameye, M., Mcguire, M.A., Steppe, K., 2015. Responses of tree species to heat waves and extreme heat events: tree response to extreme heat. Plant Cell Environ. 38 (9), 1699–1712. https://doi.org/10.1111/pce.12417.

van Meeningen, Y., Schurgers, G., Rinnan, R., Holst, T., 2016. BVOC emissions from English oak (Quercus robur) and European beech (Fagus sylvatica) along a latitudinal gradient. Biogeosciences 13, 6067–6080. https://doi.org/10.5194/bg-13-6067-2016.

Vigouroux, C., Langerock, B., Bauer Aquino, C.A., Blumenstock, T., Cheng, Z., De Mazière, M., De Smedt, I., Grutter, M., Hannigan, J.W., Jones, N., Kivi, R., Loyola, D., Lutsch, E., Mahieu, E., Makarova, M., Metzger, J.-M., Morino, I., Murata, I., Nagahama, T., Notholt, J., Ortega, I., Palm, M., Pinardi, G., Röhling, A., Smale, D., Stremme, W., Strong, K., Sussmann, R., Té, Y., van Roozendael, M., Wang, P., Winkler, H., 2020. TROPOMI–Sentinel-5 Precursor formaldehyde validation using an extensive network of ground-based Fourier-transform infrared stations. Atmos. Meas. Tech. 13 (7), 3751–3767. https://doi.org/10.5194/amt-13-3751-2020.

Watson, D.J., 1947. Comparative physiological studies on the growth of field crops: I. Variation in net assimilation rate and leaf area between species and varieties, and within and between years. Ann. Bot. 11 (No. 41), 41–76.

Wilkinson, M.J., Monson, R.K., Trahan, N., Lee, S., Brown, E., Jackson, R.B., Polley, H.W., Fay, P.A., Fall, R., 2009. Leaf isoprene emission rate as a function of atmospheric CO_2 concentration. Global Change Biol. 15 (5), 1189–1200. https://doi.org/10.1111/j.1365-2486.2008.01803.x.

World Meteorological Organization, 2012. Standardized precipitation index user guide WMO-No. 1090. https://library.wmo.int/doc_num.php?explnum_id=7768. last access: 17 April 2023.

Yan, K., Park, T., Yan, G., Chen, C., Yang, B., Liu, Z., Nemani, R., Knyazikhin, Y., Myneni, R., 2016a. Evaluation of MODIS LAI/FPAR product collection 6. Part 1: consistency and improvements. Rem. Sens. 8, 359. https://doi.org/10.3390/rs8050359.

Yan, K., Park, T., Yan, G., Liu, Z., Yang, B., Chen, C., Nemani, R., Knyazikhin, Y., Myneni, R., 2016b. Evaluation of MODIS LAI/FPAR product collection 6. Part 2:

validation and intercomparison. Rem. Sens. 8, 460. https://doi.org/10.3390/rs8060460.

Zheng, Y., Unger, N., Tadić, J.M., Seco, R., Guenther, A.B., Barkley, M.P., Potosnak, M.J., Murray, L.T., Michalak, A.M., Qiu, X., Kim, S., Karl, T., Gu, L., Pallardy, S.G., 2017. Drought impacts on photosynthesis, isoprene emission and atmospheric formaldehyde in a mid-latitude forest. Atmos. Environ. 167, 190–201. https://doi.org/10.1016/j.atmosenv.2017.08.017.

Zhu, L., Jacob, D.J., Kim, P.S., Fisher, J.A., Yu, K., Travis, K.R., Mickley, L.J., Yantosca, R. M., Sulprizio, M.P., De Smedt, I., Abad, G.G., Chance, K., Li, C, Ferrare, R., Fried, A., Hair, J.W., Hanisco, T.F., Richter, D., Scarino, A.J., Walega, J., Weibring, P., Wolfe, G.M., 2016. Observing atmospheric formaldehyde (HCHO) from space: validation and intercomparison of six retrievals from four satellites (OMI, OME2A, GOME2B, OMPS) with SEAC 4 RS aircraft observations over the Southeast US. Atmos. Chem. Phys. Discuss. 1–24. https://doi.org/10.5194/acp-2016-162.